

---

# Learning to Focus Synthetic Aperture Radar On-line with State-Space Models

---

**Sebastian Fieldhouse\***

College of Semiconductor Research  
National Tsing Hua University  
sebastianfieldhouse.2@gmail.com

**Roberto Del Prete\***

$\Phi$ -lab, European Space Agency (ESA)  
roberto.delprete@esa.int

**Gabriele Daga**

$\Phi$ -lab, European Space Agency (ESA)  
gabriele.daga@ext.esa.int

**Nathaniel Rensly**

Department of Electrical Engineering  
National Tsing Hua University  
rensly2208@gmail.com

**Gabriele Meoni**

Advanced Concepts and Studies Office,  
European Space Agency (ESA)  
gabriele.meoni@esa.int

**Kea-Tiong Tang**

Department of Electrical Engineering  
National Tsing Hua University  
kttang@ee.nthu.edu.tw

## Abstract

Conventional focusing methods for Synthetic Aperture Radar (SAR) employ block processing efficiently but remain latency-heavy processes that prevent the realisation of a closed-loop cognitive SAR vision system. We present the first Online SAR Processor (OSP), an online image-formation framework that treats SAR sensing as a stream and produces focused SAR image output line by line during acquisition. OSP uses a tiny state-space surrogate model trained with teacher-student distillation and multi-stage losses. We evaluate the method on 300GB of SAR data from Maya4, a Sentinel-1-derived dataset containing raw, range-compressed, range-cell-migration-corrected, and azimuth-compressed products. Relative to a linewise digital-signal-processing baseline, OSP delivers approximately  $70\times$  lower latency and  $130\times$  lower memory use; on a single AMD CPU core it processes one row in 16 ms with a memory footprint of 6 MB whilst maintaining a focusing quality high enough to support downstream decisions, which we illustrate with vessel detection and flood-mapping tasks.

**Keywords:** synthetic aperture radar; sequence models; image formation.

## 1 Introduction

Synthetic aperture radar (SAR) is an active sensing modality that forms high-resolution images by transmitting microwave pulses from a moving platform, such as a plane or satellite, and recording the echoes reflected from the scene as the platform moves [1–3] (Figure 1). Rather than relying on a physically large antenna, SAR synthesizes a long aperture from the motion of the sensor, which enables fine azimuth resolution even from compact airborne or spaceborne platforms [1, 4]. Because they operate at microwave frequencies, SAR systems can image the Earth during day and night and are substantially less affected by cloud cover or adverse weather than optical sensors [2, 3]. Cognitive Radar (CR), as introduced by Haykin et al. [5], is a concept that describes a perception–action loop in

---

\*These authors contributed equally to this work.

which a radar adapts its parameters – beam steering, waveform, or PRF – based on feedback from the observed environment [3]. Applying the closed-loop principle to SAR (CSAR) is compelling because SAR imaging is inherently subject to coverage–resolution trade-offs [1, 2]: wide-swath modes enable rapid search, whereas narrow-swath/spotlight modes provide higher resolution for detailed inspection [4, 6]. However, in practice, closing the loop is difficult because raw SAR measurements must be focused before they become interpretable, and conventional focusing pipelines are computationally expensive and introduce substantial latency [2, 7, 8].

In order to address these limitations and take a step towards a CSAR system, this work makes the following contributions:

- We re-formulate SAR image formation as online inference problem under the linear synthetic aperture assumption.
- We introduce the very first Online SAR Processor (OSP), a state-space surrogate for line-by-line azimuth focusing with fixed-size recurrent state,  $\sim 200$  trainable parameters, and an explicit deployment mode that processes each incoming row without storing the full aperture.
- We define an azimuth-focusing training loss that combines pointwise reconstruction with physics-constrained terms.
- We train the compact student model using knowledge distillation from a higher-capacity reference model obtained by multi-stage optimisation.
- We demonstrate a downstream proof-of-concept for low-latency decision support by applying CFAR-based vessel detection and flood segmentation to OSP-focused outputs in a line-by-line fashion.

## 2 Related Work

We position our contribution between (i) classical SAR image formation pipelines and (ii) modern sequence models for long-range operators.

### 2.1 SAR Image Formation

SAR image formation maps raw complex phase history to a reflectivity image by compensating range migration, azimuth phase evolution, motion errors, and system-dependent distortions. Classical frequency-domain processors perform matched filtering using FFTs in fast and slow time, with geometry-dependent phase corrections and re-sampling. The RDA separates focusing into range compression, RCMC, and azimuth compression, and remains standard for stripmap data under moderate squint and bandwidth assumptions [2, 1, 3]. The CSA avoids explicit RCMC interpolation through chirp scaling and phase multiplications [2, 9], while  $\omega$ - $k$  / RMA uses Stolt mapping to handle wide-angle spotlight and large-bandwidth data when its assumptions hold [4, 7, 2, 3]. Polar-format and range-stack methods provide related spatial-frequency re-gridding strategies for spotlight data [6]. Time-domain backprojection directly evaluates the focusing integral by accumulating phase-corrected pulse contributions at each image location. It is robust to wide-angle collections, topography, and non-ideal trajectories, but computationally costly without factorized, subaperture, or parallel variants [4, 7, 8]. Fast and subaperture methods can reduce latency and emit partial image updates, but they remain explicit aperture-integration algorithms whose memory and intermediate products depend on aperture support, scene geometry, and resolution. Real-time and on-board SAR processing has largely focused on accelerating classical pipelines. FPGA, GPU, and embedded implementations of RDA, CSA, SPECAN, backprojection, and related methods use pipelined FFTs, reduced precision, hardware-aware memory layouts, and parallel scheduling to lower latency and downlink burden [10–14]. However, this notion of real time is mainly throughput-oriented: processing is accelerated once the required aperture support is available. Here, we instead ask whether azimuth compression itself can be approximated by a learned causal recurrence with aperture-independent state, enabling linewise inference during acquisition. ML-based SAR methods learn priors, operators, or data-to-image mappings [15–18], but typically operate offline on full arrays, patches, or focused products.

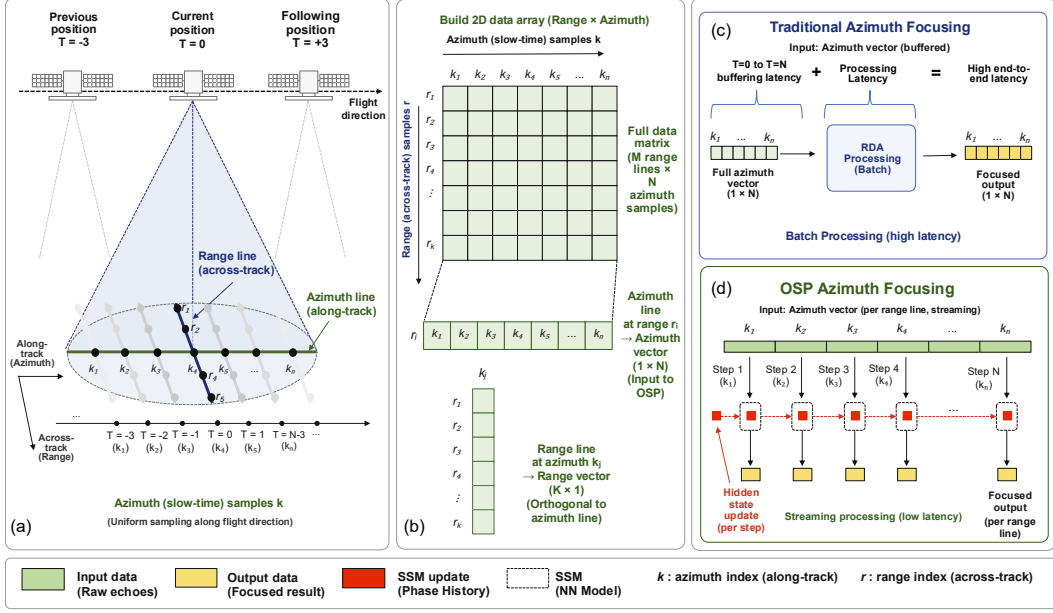


Figure 1: Streaming SAR image formation with the Online SAR Processor (OSP). (a) The platform samples the scene sequentially along slow time, indexed by pulse/azimuth index  $k$ , while each received pulse contains fast-time samples over range bins  $r$ . (b) Stacking pulses yields a complex phase-history matrix whose rows are input range vectors  $z_{k,:}$  and whose columns are azimuth sequences  $z_{1:k,r}$  at fixed range bin. (c) Conventional RDA-style azimuth focusing requires the aperture support needed by the matched-filter/FFT operations before the corresponding focused output can be formed; its end-to-end latency therefore includes aperture-buffering delay plus compute time. (d) OSP replaces the learned azimuth-focusing stage with a causal state-space recurrence applied independently to each range-bin sequence. At pulse  $k$ , the current sample  $z_{k,r}$  and range feature  $p_r$  update a range-specific hidden state,  $s_{k,r} = g_\theta(s_{k-1,r}, z_{k,r}, p_r)$ , followed by the shared readout  $\hat{x}_{k,r} = h_\theta(s_{k,r})$ . The parameters are shared across all range bins, while the hidden states remain range-bin specific. Running this recurrence for all  $r$  emits the focused row  $\hat{x}_{k,:}$ : as new pulses arrive, using fixed per-range-bin state rather than a full azimuth-aperture buffer in the learned focusing stage.

## 2.2 Sequence models for physical 1D operators

Learning-based components that operate on raw or partially processed radar signals are naturally framed as sequence-modeling problems, and the main architectural families differ primarily in inductive bias and scaling behavior. Classical RNNs and gated variants such as LSTMs and GRUs model sequences through hidden-state recursion with bounded memory [19, 20]; however, their performance is known to be limited on very-long sequences. Transformer models instead calculate the relationship between all tokens in a sequence directly via self-attention, making them more performative in long sequence tasks, however the computation and memory cost of self-attention scale poorly with the sequence length: in the canonical formulation the memory and computation cost scale as  $\mathcal{O}(L^2)$  with the sequence length  $L$  [21]; FlashAttention improves this memory cost to  $\mathcal{O}(L)$  [22]. Modern SSM models such as s4 or s5 represent a sequence through a latent dynamic state driven by the input and read out to the output. They are especially attractive for 1D signal processing because inference can be  $\mathcal{O}(L)$  via a scan/recurrence and they have a fixed memory footprint of  $\mathcal{O}(1)$ . Additionally, they have been shown to have high performance even when used on very long sequence tasks [23].

### 3 Methodology

#### 3.1 SAR Acquisition Geometry

Referring to Figure 1, we consider stripmap acquisition, in which the platform translates along the azimuth direction and the antenna beam is held fixed in azimuth relative to the platform, rather than being steered to dwell on a scene patch as in spotlight imaging. Each received pulse provides samples in fast time, corresponding to range, and successive pulses sample slow time, corresponding to azimuth. Stacking the pulses therefore yields a two-dimensional complex phase-history array indexed by range bin and slow-time/pulse index. Each pulse gives a range profile, and the same target is observed over many pulses as its sensor-target distance changes. Because a target drifts across range bins during the aperture [2], classical processors explicitly compensate this effect through RCMC or related re-sampling operations. In this work we don’t compensate for this drift but we assume a moderate-aperture stripmap setting in which the synthetic aperture can be considered linear. This motivates the OSP view of azimuth as an ordered slow-time sequence, where target information accumulates progressively across pulses.

#### 3.2 Online SAR Processor

Conceptually, our OSP operates in three steps: (a) a complex range line is acquired, (b) range compression is applied using conventional DSP operations, and (c) a compact neural state-space model incrementally performs azimuth focusing by updating a recurrent state that encodes the relevant phase-history context. Instead of buffering a large azimuth aperture and applying explicit slow-time FFTs, the processor applies the same causal recurrent operator to each range cell in parallel. For range bin  $r$  at pulse  $k$ , let  $z_{k,r} \in \mathbb{R}^2$  denote the real/imaginary representation of the current complex sample. OSP maintains a hidden state  $s_{k,r} \in \mathbb{R}^d$  and updates it as

$$s_{k+1,r} = g_\theta(s_{k,r}, z_{k,r}, p_r), \quad \hat{x}_{k,r} = h_\theta(s_{k+1,r}), \quad (1)$$

where  $p_r$  is an optional normalized range-position feature and the parameters of  $g_\theta$  and  $h_\theta$  are shared across all range bins. This parameter sharing is what allows the model to focus an entire line while keeping the number of trainable weights extremely small. In practice,  $g_\theta$  is implemented as a lightweight input projection followed by a stack of S4D structured state-space layers and  $h_\theta$  is a narrow output head that predicts the focused complex response. The deployable student contains only 208 trainable parameters, yet still maintains enough dynamic state to model long azimuth responses. We initialize the recurrent kernels with the S4D-Lin parameterization [24]. To stabilize the training of this very compact model, we adopt a distillation (Section 4.3) approach: first, a higher-capacity teacher is optimized for reconstruction quality under the azimuth-focusing objective described in Section 4.1, and then the compact student is then trained to reproduce both the focused target and the teacher’s response. It is worth noting that during training we process finite azimuth strips in mini-batches using the convolutional mode of S4D, but at deployment we switch to the recurrent form of the model and retain only the current hidden state and the newest pulse. Training details and reproducibility details are given in appendix A.4

### 4 Experiments

We evaluate OSP using a fixed Maya4 split, deterministic strip sampling, origin-preserving complex normalization, and a recurrent deployment protocol matching the causal SSM boundary conditions used during training. *Maya4* [25] is a Sentinel-1-derived dataset of 2TB, which we split into training, validations and test data, that provides intermediate SAR representations from Level 0 raw measurements to Level 1 focused imagery. Using the RDA as the reference pipeline, each sample is stored as four aligned stages: *raw*, *range-compressed* (RC), *range-cell-migration-corrected* (RCMC), and *azimuth-compressed* (AZ).

#### 4.1 Azimuth Focusing Loss

The azimuth-focusing loss is a central contribution of this study and is designed specifically to model SAR structure along the azimuth dimension, and it is defined as follows. Let  $\hat{z} \in \mathbb{C}^L$  be the predicted azimuth strip and  $z \in \mathbb{C}^L$  the ground-truth strip after inverse min-max normalization. Writing

Table 1:  $\mathcal{L}_{\text{AF}}$  sub-terms expansion

TERM	DEFINITION	WEIGHT	TERM	DEFINITION	WEIGHT
$\mathcal{L}_{\text{complex}}$	$\frac{1}{L} \ \hat{z} - z\ _1$	$w_c$	$\mathcal{L}_{\text{log amp}}$	$\frac{1}{L} \ \ell - \ell^*\ _1$	$w_{\text{log}}$
$\mathcal{L}_{\text{amp-corr}}$	$1 - \rho(a, a^*)$	$w_{\text{ac}}$	$\mathcal{L}_{\text{tail}}$	$ \log \frac{Q_{.95}(a)}{Q_{.95}(a^*)}  + \frac{1}{2}  \log \frac{Q_{.99}(a)}{Q_{.99}(a^*)} $	$w_{\text{tail}}$
$\mathcal{L}_{\text{az-grad}}$	$\frac{1}{L-1} \ \Delta \ell - \Delta \ell^*\ _1$	$w_{\nabla}$	$\mathcal{L}_{\text{az-psd}}$	$\ P(\ell) - P(\ell^*)\ _1$	$w_{\text{psd}}$
$\mathcal{L}_{\text{focus-width}}$	$\frac{ W(\ell) - W(\ell^*) }{W(\ell^*) + \varepsilon}$	$w_{\text{fw}}$	$\mathcal{L}_{\text{az-edge}}$	$\frac{1}{L-2} \ \Delta^2 \ell - \Delta^2 \ell^*\ _1$	$w_{\text{edge}}$

$a = |\hat{z}|$ ,  $a^* = |z|$ ,  $\ell = \log(a + \varepsilon)$ , and  $\ell^* = \log(a^* + \varepsilon)$ , the optimized objective is

$$\begin{aligned} \mathcal{L}_{\text{AF}} = & w_c \mathcal{L}_{\text{complex}} + w_{\text{log}} \mathcal{L}_{\text{log amp}} + w_{\text{ac}} \mathcal{L}_{\text{amp-corr}} + w_{\text{tail}} \mathcal{L}_{\text{tail}} \\ & + w_{\nabla} \mathcal{L}_{\text{az-grad}} + w_{\text{psd}} \mathcal{L}_{\text{az-psd}} + w_{\text{fw}} \mathcal{L}_{\text{focus-width}} + w_{\text{edge}} \mathcal{L}_{\text{az-edge}}. \end{aligned} \quad (2)$$

Here  $w_c$ ,  $w_{\text{log}}$ ,  $w_{\text{ac}}$ ,  $w_{\text{tail}}$ ,  $w_{\nabla}$ ,  $w_{\text{psd}}$ ,  $w_{\text{fw}}$ , and  $w_{\text{edge}}$  are non-negative scalar weights. We use  $\rho(\cdot, \cdot)$  for the amplitude-correlation coefficient,  $Q_p(\cdot)$  for the empirical  $p$ -quantile,  $\Delta$  and  $\Delta^2$  for first- and second-order finite differences along azimuth,  $P(\cdot)$  for the normalized one-dimensional azimuth PSD estimate evaluated on normalized frequencies  $f \in [0.15, 0.5]$ , and  $W(\cdot)$  for an autocorrelation-derived focus-width statistic;  $\varepsilon > 0$  is a small numerical-stability constant used in the logarithm and denominator terms. We summarize each of the subterms of  $\mathcal{L}_{\text{AF}}$  in Table 1, and further elaborate in Appendix A. The complex term  $\mathcal{L}_{\text{complex}}$  is the primary data-fidelity anchor: because it acts directly in complex space, it penalizes residual phase and amplitude mismatch before magnitude-only surrogates can mask physically incorrect solutions. The log-amplitude term  $\mathcal{L}_{\text{log amp}}$  operates on a compressed dynamic range, which makes multiplicative radiometric errors more nearly additive and prevents optimization from being dominated by a small number of very bright scatterers. The amplitude-correlation term  $\mathcal{L}_{\text{amp-corr}}$  is comparatively insensitive to global rescaling, so it emphasizes agreement in azimuthal response shape rather than absolute gain. The tail term  $\mathcal{L}_{\text{tail}}$  explicitly matches upper quantiles, preserving rare high-intensity responses that are operationally important but can otherwise be suppressed by objectives that mainly optimize average error. The azimuth-gradient term  $\mathcal{L}_{\text{az-grad}}$  matches first-order log-amplitude derivatives and therefore sharpens rise/fall transitions associated with well-focused impulse responses, while the PSD-band term  $\mathcal{L}_{\text{az-psd}}$  constrains spectral energy in the informative mid/high azimuth band and acts as a frequency-domain safeguard against excessive low-pass smoothing. The focus-width term  $\mathcal{L}_{\text{focus-width}}$  penalizes mainlobe broadening through an autocorrelation-derived width statistic that serves as a compact proxy for focusing concentration, and the azimuth-edge term  $\mathcal{L}_{\text{az-edge}}$  matches second-order differences to regulate local curvature, suppress ringing, and reject both over-smoothed and oscillatory solutions.

## 4.2 Multi-Stage Teacher Optimization

Teacher selection was carried out as a staged optimization procedure over a shared Stage-0 baseline. The baseline is included explicitly in Table 2 because all reported improvements are computed relative to it. All completed runs were evaluated using RMSE  $R$ , amplitude correlation  $C$ , and complex coherence  $Q$ . The setting selected at each stage minimizes the rank score

$$s(x) = \frac{1}{2} (\text{rk}_R(x) + \text{rk}_C(x)), \quad (3)$$

where  $\text{rk}_R$  is the dense rank of RMSE in ascending order and  $\text{rk}_C$  is the dense rank of amplitude correlation in descending order. Complex coherence is reported as an auxiliary diagnostic and is not used directly in the rank score. Phase preservation for phase-critical products, such as interferometry, is left to future work. When we refer to “selectivity” in the ablations, we mean a lightweight input-conditioned gate in our OSP block, not the full selective-scan architecture introduced by Mamba [26]. The gate is used only to test whether modest input-dependent modulation of the state update improves the azimuth-focusing surrogate. The staged design separates architecture, regularization, and loss-weight effects. Stage I keeps the loss fixed and varies only model capacity and training-control parameters. As illustrated in Figure 2, increasing capacity beyond the Stage-0 reference does not yield a consistent improvement. The best Stage I run instead changes regularization, selecting dropout = 0.10 while retaining the baseline loss weights. This improves RMSE by +1.15% and amplitude correlation by +3.10%, indicating that regularization is a more productive first-order adjustment

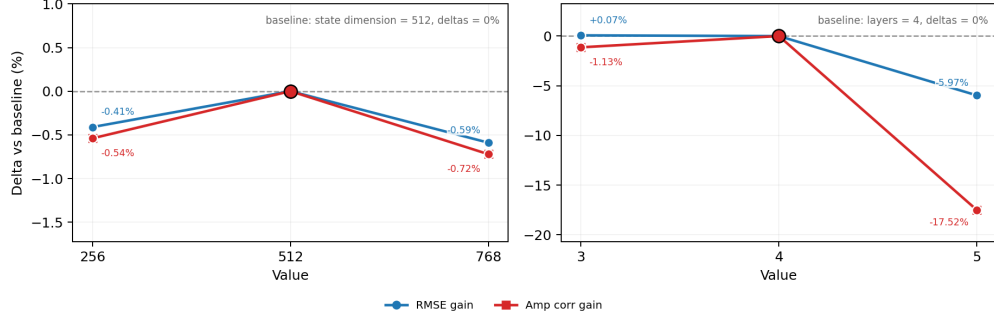


Figure 2: Capacity ablation for the high-capacity Stage-0 baseline. The left panel varies state dimension (baseline: 512); the right panel varies layer count (baseline: 4). Values show percentage deltas relative to the baseline for RMSE and amplitude-correlation gains; negative means worse. Alternative configurations were sub-optimal or comparable, supporting the chosen baseline.

Table 2: Unified summary of the preliminary recurrent-baseline screening, Stage-0 SSM baseline, and staged teacher sweep.  $N$  is the number of runs in the stage. The LSTM/GRU screen is listed for completeness.

Stage	$N$	Swept parameters	Selected setting	$R \downarrow$	$C \uparrow$	$Q \uparrow$	$\Delta_R^\ddagger$	$\Delta_C^\ddagger$
NA <sup>†</sup>	16	Sequence-model debug sweep: model $\in$ {LSTM, GRU}, hidden dimension $\in$ {6, 9}, layers $\in$ {1, 2}, learning rate $\in$ $\{10^{-4}, 3 \times 10^{-4}\}$ . All runs used input dimension 3, output dimension 1, unidirectional recurrence, and dropout 0.0.	Screening only; no teacher selected from this grid. Separate production recurrent baselines used GRU $h = 11, L = 4$ , dropout 0.05, and LSTM $h = 9, L = 4$ , dropout 0.05.				failed to converge.	
0*	1	Development OSP baseline; no sweep.	$l_r = 4.0 \times 10^{-4}$ ; $d_{state} = 512$ , $L = 4$ ; dropout = 0.05; selectivity = OFF, skip = ON; $w_{log} = 0.22$ , $w_{ac} = 0.20$ , $w_{tail} = 0.14$ , $w_{\nabla} = 0.12$ , $w_{psd} = 0.08$ , $w_{fw} = 0.02$ , $w_{edge} = 0.00$ .	7837.360	0.2063	0.2806	0.00%	0.00%
I	9	Architecture/control: state dimension {256, 512, 768}, layers {3, 4, 5}, dropout {0, 0.05, 0.10}, selectivity on/off, skip on/off.	Dropout = 0.10; baseline loss weights.	7747.460	0.213	0.291	+1.15%	+3.10%
II	27	Early loss and control combinations: $\eta$ , $w_{log}$ , $w_{ac}$ , $w_{edge}$ , dropout, selectivity.	Dropout = 0.10; selectivity on; $w_{ac} = 0.22$ .	<b>7745.140</b>	0.215	0.299	+1.18%	+4.36%
III	6	Local two-parameter loss refinement: $\eta \in \{3.8, 4.0, 4.2\} \times 10^{-4}$ and $w_{log} \in \{0.20, 0.22\}$ .	$\eta = 3.8 \times 10^{-4}$ ; $w_{log} = 0.20$ .	7816.940	0.207	0.282	+0.26%	+0.48%
IV	16	Local loss-balance refinement: $\eta$ , $w_{log}$ , $w_{ac}$ , and $w_{edge}$ .	$\eta = 3.8 \times 10^{-4}$ ; $w_{log} = 0.24$ ; $w_{ac} = 0.20$ ; $w_{edge} = 0.01$ .	7808.830	0.217	0.298	+0.37%	+5.28%
V	92	Family-wise search: dropout, selectivity, $\eta$ , $w_c$ , $w_{log}$ , $w_{ac}$ , $w_{tail}$ , $w_{\nabla}$ , $w_{psd}$ , $w_{fw}$ , $w_{edge}$ , and adaptive reweighting.	Final teacher: $w_c = 0.04$ , $w_{log} = 0.18$ , $w_{ac} = 0.18$ , $w_{tail} = 0.12$ , $w_{\nabla} = 0.24$ , $w_{psd} = 0.04$ , $w_{fw} = 0.04$ , $w_{edge} = 0.08$ , $\epsilon = 10^{-3}$ .	7752.610	<b>0.222</b>	<b>0.303</b>	+1.08%	<b>+7.51%</b>

<sup>‡</sup> We report normalized signed deltas  $\Delta_R(x) = 100(R_0 - R(x))/R_0$  and  $\Delta_C(x) = 100(C(x) - C_0)/C_0$ . Larger  $\Delta_R$  means lower RMSE, and larger  $\Delta_C$  means higher amplitude correlation.

than simply increasing state dimension or depth. Stage II begins the loss-design sweep. It combines the successful dropout setting with selectivity and small perturbations of the amplitude-structure terms in  $\mathcal{L}_{AF}$ . The selected run enables selectivity and increases the amplitude-correlation weight from the Stage-0 value  $w_{ac} = 0.20$  to  $w_{ac} = 0.22$ . Among the stage representatives, this yields the strongest RMSE improvement,  $\Delta_R = +1.18\%$ , while also increasing amplitude correlation by  $\Delta_C = +4.36\%$ . Stages III and IV refine the loss surface locally. Stage III sweeps only  $\eta$  and  $w_{log}$ , yielding only a modest gain over the baseline. This suggests that log-amplitude calibration alone is insufficient for preserving focused azimuth structure. Stage IV adds  $w_{ac}$  and the azimuth-edge weight  $w_{edge}$ , increasing amplitude correlation to  $\Delta_C = +5.28\%$ . This supports the interpretation that azimuth focusing quality depends on balancing log-amplitude calibration, amplitude-correlation alignment, and edge-sensitive structural terms. The final stage expands the most promising region into explicit loss families, including local-basin variants, selectivity-correlation variants, learning-rate-transfer variants, secondary-loss variants over  $w_{tail}$ ,  $w_{\nabla}$ ,  $w_{psd}$ , and  $w_{fw}$ , adaptive-reweighting

variants, high-edge variants, and amplitude-correlation/edge-balanced variants. The selected teacher, reported Table 2, achieves the highest amplitude correlation and complex coherence among the stage representatives while still improving RMSE relative to the Stage-0 baseline.

### 4.3 Teacher–Student Distillation

The staged sweep selected a high-capacity teacher  $T_\phi$ , trained with the azimuth-focusing loss and used only for distillation. The deployable Online SAR Processor is the compact student  $S_\theta$ , which keeps the same complex I/O interface but uses the recurrent state-space stack needed for linewise online inference. Distillation is used as both a compression mechanism and an optimization stabilizer: the student is not trained to discover the full azimuth-compression operator from the hard AZ target alone, but is also given a smooth complex-valued surrogate response from the teacher. For an inverse-

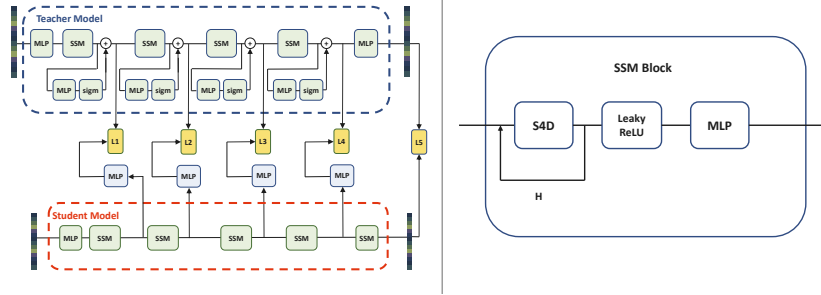


Figure 3: Teacher–student distillation architecture for OSP. The offline teacher uses a higher-capacity SSM stack to learn a stable complex-valued RC-to-AZ focusing map under the azimuth-focusing objective. During distillation, the teacher is frozen and provides soft complex-field supervision to the compact student. The student preserves the same input–output interface as the teacher, but uses a much smaller causal SSM stack that can be executed in recurrent mode for fixed-state online inference.

normalized input azimuth strip  $u$ , reference AZ strip  $z$ , teacher prediction  $\hat{z}_T = T_\phi(u)$ , and student prediction  $\hat{z}_S = S_\theta(u)$ , the teacher parameters are frozen and the student is trained with

$$\mathcal{L}_{\text{student}} = \mathcal{L}_{\text{AF}}(\hat{z}_S, z) + \lambda_{\text{KD}} \mathcal{D}(\hat{z}_S, \text{sg}[\hat{z}_T]), \quad (4)$$

where  $\text{sg}[\cdot]$  denotes stop-gradient and  $\mathcal{L}_{\text{AF}}$  is the physically motivated azimuth-focusing loss defined in Eq. 2. With reference to Figure 3, the distillation discrepancy is evaluated in the same complex domain as the reconstruction loss,

$$\begin{aligned} \mathcal{D}(a, b) = & \alpha_c \|a - b\|_1 + \alpha_\ell \|\log(|a| + \epsilon) - \log(|b| + \epsilon)\|_1 \\ & + \alpha_\rho (1 - \rho(|a|, |b|)) + \alpha_\phi (1 - \cos(\angle a - \angle b)). \end{aligned} \quad (5)$$

The first term transfers the teacher’s complex response, the log-amplitude and correlation terms transfer radiometric structure while being less sensitive to global scale, and the circular phase term avoids an artificial penalty at the  $-\pi/\pi$  wrap. The hard-target term in Eq. (4) prevents the student from inheriting teacher-specific bias, while the teacher term regularizes the severely under-parameterized recurrent model toward a physically plausible focusing operator. After training,  $T_\phi$  is discarded; only  $S_\theta$  is used in the online processor. Table 3 summarizes the quantitative teacher–student gap on the held-out set. The distilled student largely preserves aggregate pointwise accuracy: RMSE increases by only 2.16%, while phase MAE and phase RMSE increase by 11.2% and 8.51%, respectively. The larger degradation is instead in structured complex fidelity. The representative qualitative results in Figure 4 explain the aggregate teacher–student gap. The teacher predictions preserve the dominant morphology of both held-out scenes: the agricultural field pattern in product 0042df and the coastal/water structure in product 00413d remain spatially aligned with the AZ references. This is reflected in the overlaid amplitude-correlation scores, where the teacher outperforms the student in both examples (0.540 versus 0.262 for 0042df, and 0.478 versus 0.262 for 00413d). The student recovers the coarse focused layout, but its output is less structurally faithful. The practical implication of this is the student model is good enough for rough amplitude-based applications but is not yet reliable for tasks that need accurate phase or calibrated complex outputs.

Table 3: Teacher–student comparison on the test set ( $n = 25,600$  complex samples) and final loss/distillation hyperparameters. Panel A reports scalar reconstruction error, amplitude calibration, complex coherence, and phase fidelity. Panel B reports the ground-truth-aligned azimuth-focusing loss weights and the student-only distillation coefficients. The student remains close to the teacher in pointwise error metrics, but loses substantial correlation and coherence, indicating that the main distillation gap is structured complex fidelity rather than aggregate RMSE.

A. Test-set reconstruction and coherence metrics							
Metric	Teacher	Student	$\Delta$	Metric	Teacher	Student	$\Delta$
RMSE ( $\downarrow$ )	<b>7753</b>	7920	+2.16%	Complex coh. ( $\uparrow$ )	<b>0.303</b>	0.147	−51.5%
Amp. corr. ( $\uparrow$ )	<b>0.222</b>	0.099	−55.3%	Phase coh. ( $\uparrow$ )	<b>0.240</b>	0.107	−55.5%
Mean amp. err. ( $\downarrow$ )	<b>0.080</b>	0.148	+85.3%	Phase MAE ( $\downarrow$ )	<b>76.2</b>	84.8	+11.2%
P95 amp. err. ( $\downarrow$ )	0.069	<b>0.017</b>	−75.7%	Phase RMSE ( $\downarrow$ )	<b>91.5</b>	99.3	+8.51%

B. Final teacher/student loss and distillation hyperparameters																
Model	$w_c$	$w_{\log}$	$w_{ac}$	$w_{tail}$	$w_{\nabla}$	$w_{psd}$	$w_{fw}$	$w_{edge}$	$\epsilon$	PSD band	$W_{info}$	$\lambda_{KD}$	$\alpha_c$	$\alpha_\ell$	$\alpha_\rho$	$\alpha_\phi$
Teacher	0.04	0.18	0.18	0.12	0.24	0.04	0.04	0.08	$10^{-3}$	[0.15, 0.50]	$0.75 + 0.50 \tilde{I}$	0	0	0	0	0
Student	0.35	0.08	0.08	0.03	0.02	0.01	0.00	0.005	$10^{-3}$	[0.15, 0.50]	same as teacher	0.05	0.25	0	0.08	0.05

Notes. For  $\downarrow$  metrics, positive  $\Delta$  indicates larger error; for  $\uparrow$  metrics, negative  $\Delta$  indicates lower fidelity. The amplitude errors are absolute deviations from the ideal amplitude ratio of one.  $W_{info}$  is the per-strip informativeness weight, denoted  $W$  in the experiment logs (see Appendix A).

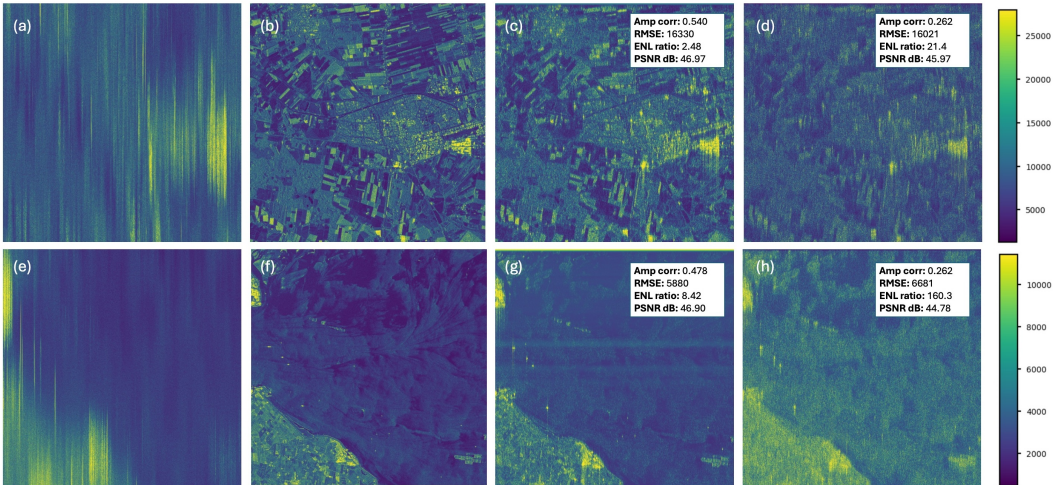


Figure 4: Teacher–student inference on two held-out Sentinel-1-derived SAR strips. The top row corresponds to product 0042df and the bottom row to product 00413d. Panels (a,e) are the RC inputs, (b,f) are the AZ references, (c,g) are teacher outputs, and (d,h) are student outputs. Metrics overlaid on the prediction panels are computed against the AZ reference: amplitude correlation, RMSE, equivalent-number-of-looks ratio, and PSNR. The teacher more closely preserves the reference scene morphology and radiometric structure, while the compact student recovers the coarse focused layout but exhibits lower amplitude correlation and stronger strip-wise artifacts.

#### 4.4 Potential Online Applications

An important test of SAR focusing quality is whether the focused output supports simple downstream decisions. We therefore experiment with two (of many) potential downstream tasks that would benefit from rapid focusing using OSP; these two applications are CFAR vessel detection and fixed threshold flood mapping, the results of which we show in figure 5. Vessel detection is important for preservation of protected maritime areas where fishing and shipping vessel passage are restricted. By providing a rapid localization of a vessel in a restricted maritime area using OSP and line-wise CFAR, it could be possible for the SAR system to take a second, high-resolution scan via spotlight whilst still flying overhead the detected vessel of interest for identification purposes and improve enforcement on fishing restrictions etc. As a proof-of-concept we apply a line-wise CFAR detector to an OSP-focused scene over Porto de Santos, Brazil. Rapid flood-mapping is also another time-sensitive downstream task

which would benefit from rapid focusing to support early situational awareness and sensor-tasking decisions. As an example, we implement a fixed-threshold based segmentation of an OSP-focused scan of lakes in the area around Sao Paolo, also presented in figure 5. Our intent is not to present a complete segmentation system or vessel detection system, rather demonstrate that many applications would benefit from rapid focusing for re-tasking and that the output quality of OSP is high enough to achieve this.

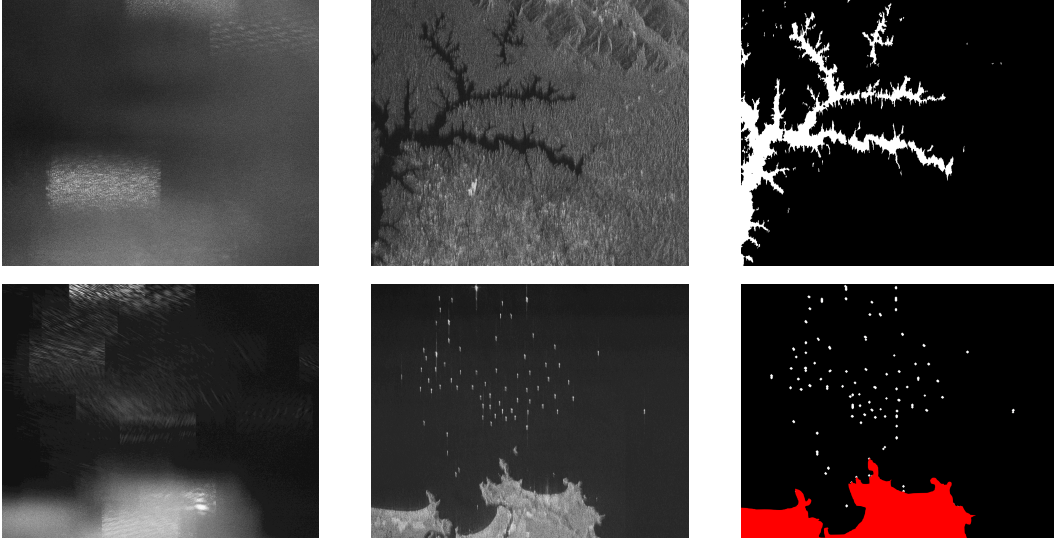


Figure 5: (Top) Demonstration of constant threshold water segmentation with applications such as flood detection - scan captured over Sao Paolo. (Top Left): raw SAR data as received by satellite. (Top Center): focused output produced by OSP. (Top Right): Segmentation map of water coverage obtained using single value thresholding. (Bottom) Demonstration of vessel detection using OSP over Porto de Santos, Brazil. (Bottom Left): raw SAR data as received by the satellite. (Bottom Center): focused output produced by OSP; bright point responses correspond to strong scatterers, including vessels and port infrastructure. (Bottom Right): vessel-like detections obtained with a linewise CFAR detector using a rolling buffer of 77 range lines. False positives over land are suppressed using geographic masking, shown in red.

## 5 Discussion

The central result of this paper is that, after standard front-end preprocessing, a substantial portion of the azimuth-focusing operator can be represented as a compact causal dynamical system. To highlight the advantages of our Online Processor, we compare our proposed method against two implementations of the RDA algorithm, one being the commonly used "batched" RDA where all operations are performed in batches, and the other is a version of the RDA which relies on buffering a window of SAR history that can perform focusing of a single range line at a time that we call the linewise RDA: the comparison of these results are presented in Table 16. We state all our assumptions and derivations in Appendix C.

Due to the fact our model uses fixed memory footprint SSM layers as its backbone and does not require buffering data in the azimuth direction, we obtain a far superior memory footprint to both baselines; our online formulation also enables drastically reduced data-in-to-data-out focusing latency. We show detailed computational complexity and FLOPs derivations in Appendices C and D. We also present extended discussion including limitations, failure cases, operational considerations and robustness in Appendix G.

## 6 Conclusions

We introduce the Online SAR processor, a streaming formulation of SAR image formation in which azimuth focusing is performed incrementally via a compressed phase-history rather than after full-

Table 4: Complexity, latency, memory, and compute comparison. Lower latency, memory, and GFLOPs per row are better.

Method	Complexity	Single-line latency (ms)*	Full scan latency (ms)*	Memory footprint	GFLOPs per scan	GFLOPs per row
Traditional RDA	$\mathcal{O}(N_a N_r \log(N_a N_r))$	N/A <sup>†</sup>	<b>27,444</b>	16 GB	<b>122</b>	N/A <sup>†</sup>
Linewise RDA	$\mathcal{O}(N_a N_r N_b \log(N_b N_r))$	857 (+243) <sup>‡</sup>	17,140,000	780 MB	45,400	2.27
<i>This work</i>	$\mathcal{O}(N_a N_r \log(N_r))$	<b>15.1</b>	302,000	<b>6 MB</b>	324	<b>0.016</b>

\*Latency measured on a single core of an AMD EPYC 7343 CPU.

<sup>†</sup>Cannot be used to process individual range lines in an online manner.

<sup>‡</sup>Processing starts only after the history buffer is filled, adding delay beyond pure compute time.

aperture buffering, allowing for a much more rapid focusing than traditional techniques; we also illustrate how this could enable rapid sensor retasking in potential CSAR applications like vessel detection.

## References

- [1] John C. Curlander and Robert N. McDonough. *Synthetic Aperture Radar: Systems and Signal Processing*. Wiley, 1991.
- [2] Ian G. Cumming and Frank H. Wong. *Digital Processing of Synthetic Aperture Radar Data: Algorithms and Implementation*. Artech House, 2005.
- [3] Mark A. Richards. *Fundamentals of Radar Signal Processing*. McGraw-Hill Education, 2 edition, 2014.
- [4] William G. Carrara, Ronald S. Goodman, and Ronald M. Majewski. *Spotlight Synthetic Aperture Radar: Signal Processing Algorithms*. Artech House, 1995.
- [5] Simon Haykin. Cognitive radar: A way of the future. *IEEE Signal Processing Magazine*, 23(1): 30–40, 2006.
- [6] Charles V. Jakowatz, Daniel E. Wahl, Paul H. Eichel, Dennis C. Ghiglia, and Paul A. Thompson. *Spotlight-Mode Synthetic Aperture Radar: A Signal Processing Approach*. Kluwer Academic Publishers, 1996.
- [7] Mehrdad Soumekh. *Synthetic Aperture Radar Signal Processing with MATLAB Algorithms*. Wiley, 1999.
- [8] Lars M. H. Ulander, Hans Hellsten, and Gunnar Stenstrom. Synthetic-aperture radar processing using fast factorized back-projection. *IEEE Transactions on Aerospace and Electronic Systems*, 39(3):760–776, 2003.
- [9] Alberto Moreira, Josef Mittermayer, and Rolf Scheiber. Extended chirp scaling algorithm for air- and spaceborne sar data processing in stripmap and scansar imaging modes. *IEEE Transactions on Geoscience and Remote Sensing*, 34(5):1123–1136, 1996.
- [10] Laura Parra Garcia, Carmine Clemente, Christos Ilioudis, Gianluca Furano, Maxime Ghiglione, Ernesto Imbembo, Valentina Zancan, and Paolo Trucco. Advancements in on-board processing of synthetic aperture radar (sar) data: Enhancing efficiency and real-time capabilities. *IEEE Journal of Selected Topics in Applied Earth Observations and Remote Sensing*, 2024. doi: 10.1109/JSTARS.2024.3406155.
- [11] Yeongung Choi, Dongmin Jeong, Myeongjin Lee, Wookyung Lee, and Yunho Jung. Fpga implementation of the range-doppler algorithm for real-time synthetic aperture radar imaging. *Electronics*, 10(17):2133, 2021. doi: 10.3390/electronics10172133.
- [12] S. Mandapati. Real time floating point sar focusing on fpga. In *International Conference on Space Optics*, 2024.
- [13] Y. Xu et al. The adaptive streaming sar back-projection algorithm based on half-precision in gpu. *Electronics*, 11(18):2807, 2022. doi: 10.3390/electronics11182807.

- [14] Y. Zhang et al. A near-real-time imaging algorithm for focusing spaceborne sar data in multiple modes based on an embedded gpu. *Remote Sensing*, 17(9):1495, 2025. doi: 10.3390/rs17091495.
- [15] Bora Yonel, Volkan Cevher, Ali Cuhadar, and Muhittin Cetin. Passive sar imaging by deep unrolled optimization. In *EUSIPCO*, 2017.
- [16] Yifan Zhao et al. Deepred for sar imaging: Deep priors with plug-and-play regularization. *IEEE Transactions on Computational Imaging*, 2024.
- [17] Yifan Ji et al. Approximate observation operators with complex-valued cnns for sparse sar imaging. *IEEE Geoscience and Remote Sensing Letters*, 2024.
- [18] Xue Huang et al. Deeparnet: Learning representations from complex-valued sar data. *Remote Sensing*, 2020.
- [19] Sepp Hochreiter and Juergen Schmidhuber. Long short-term memory. *Neural Computation*, 9(8):1735–1780, 1997.
- [20] Kyunghyun Cho, Bart van Merriënboer, Dzmitry Bahdanau, and Yoshua Bengio. On the properties of neural machine translation: Encoder–decoder approaches. In *SSST-8*, 2014.
- [21] Ashish Vaswani, Noam Shazeer, Niki Parmar, Jakob Uszkoreit, Llion Jones, Aidan N. Gomez, Lukasz Kaiser, and Illia Polosukhin. Attention is all you need. In *NeurIPS*, 2017.
- [22] Tri Dao, Daniel Y. Fu, Stefano Ermon, Atri Rudra, and Christopher Ré. FlashAttention: Fast and memory-efficient exact attention with IO-awareness. In *Advances in Neural Information Processing Systems (NeurIPS)*, volume 35, 2022.
- [23] Albert Gu, Karan Goel, and Christopher Re. Efficiently modeling long sequences with structured state spaces. In *ICLR*, 2022.
- [24] Albert Gu, Ankit Gupta, Karan Goel, and Christopher Ré. On the parameterization and initialization of diagonal state space models. *Advances in Neural Information Processing Systems*, 35:35971–35983, 2022.
- [25] European Space Agency Phi-lab. Maya4. <https://huggingface.co/buckets/ESA-philab/Maya4>, 2025. Hugging Face storage bucket, accessed 2026-05-03.
- [26] Albert Gu and Tri Dao. Mamba: Linear-time sequence modeling with selective state spaces. *arXiv preprint arXiv:2312.00752*, 2023.
- [27] James W. Cooley and John W. Tukey. An algorithm for the machine calculation of complex fourier series. *Mathematics of Computation*, 19(90):297–301, April 1965. doi: 10.2307/2003354. URL <https://doi.org/10.2307/2003354>.
- [28] Daniel E. Wahl, Paul H. Eichel, Dennis C. Ghiglia, and Charles V. Jakowatz. Phase gradient autofocus—a robust tool for high resolution sar phase correction. *IEEE Transactions on Aerospace and Electronic Systems*, 30(3):827–835, 1994.

## A Reproducibility Details and Loss Implementation

**Compute environment.** Training was run on PBS gpu4\_std CUDA nodes with one GPU, 16 CPU cores, and 32GB RAM per training job. Inference and metric evaluation used one GPU, 16 CPU cores, and up to 64GB RAM. These resources describe model training and offline evaluation compute only.

### A.1 Ground-Truth-Aligned Azimuth-Focusing Loss

All loss terms are evaluated on one-dimensional azimuth strips of length  $L$ . Let  $\hat{z} \in \mathbb{C}^L$  denote the model prediction and  $z \in \mathbb{C}^L$  the target strip in the normalized training space. The physical-scale strips are obtained by inverse normalization,

$$\hat{u} = T^{-1}(\hat{z}), \quad u = T^{-1}(z),$$

where  $T^{-1}$  is the inverse of the normalization applied during data loading. We define physical amplitudes and log-amplitudes as

$$\hat{a}_j = |\hat{u}_j|, \quad a_j = |u_j|, \quad \hat{\ell}_j = \log(\hat{a}_j + \epsilon), \quad \ell_j = \log(a_j + \epsilon).$$

The implemented ground-truth-aligned objective is

$$\mathcal{L}_{\text{GT}} = w_c \mathcal{L}_c + w_{\log} \mathcal{L}_{\log} + w_{\text{ac}} \mathcal{L}_{\text{ac}} + w_{\text{tail}} \mathcal{L}_{\text{tail}} + w_{\text{grad}} \mathcal{L}_{\text{grad}} + w_{\text{psd}} \mathcal{L}_{\text{psd}} + w_{\text{fw}} \mathcal{L}_{\text{fw}} + w_{\text{edge}} \mathcal{L}_{\text{edge}}. \quad (6)$$

The complex data-fidelity term is computed in the normalized complex field,

$$\mathcal{L}_c = \frac{1}{L} \sum_{j=1}^L |\hat{z}_j - z_j| = \frac{1}{L} \sum_{j=1}^L \sqrt{(\hat{r}_j - r_j)^2 + (\hat{i}_j - i_j)^2}, \quad (7)$$

where  $\hat{z}_j = \hat{r}_j + \hat{i}_j$  and  $z_j = r_j + i_j$ . The remaining terms operate on inverse-normalized physical amplitudes or their log-amplitudes.

The log-amplitude term is

$$\mathcal{L}_{\log} = \frac{1}{L} \sum_{j=1}^L |\hat{\ell}_j - \ell_j|. \quad (8)$$

Amplitude-shape agreement is measured by the Pearson correlation of physical amplitudes,

$$\rho_a = \frac{\sum_{j=1}^L (\hat{a}_j - \bar{\hat{a}})(a_j - \bar{a})}{\sqrt{\sum_{j=1}^L (\hat{a}_j - \bar{\hat{a}})^2 \sum_{j=1}^L (a_j - \bar{a})^2 + \epsilon}}, \quad \mathcal{L}_{\text{ac}} = 1 - \text{clip}(\rho_a, -1, 1). \quad (9)$$

The tail term penalizes mismatch in rare high-amplitude responses through upper amplitude quantiles,

$$\mathcal{L}_{\text{tail}} = \left| \log \frac{q_{0.95}(\hat{a}) + \epsilon}{q_{0.95}(a) + \epsilon} \right| + \frac{1}{2} \left| \log \frac{q_{0.99}(\hat{a}) + \epsilon}{q_{0.99}(a) + \epsilon} \right|. \quad (10)$$

The first-order azimuth-gradient term matches local log-amplitude changes,

$$\mathcal{L}_{\text{grad}} = \frac{1}{L-1} \sum_{j=1}^{L-1} \left| (\hat{\ell}_{j+1} - \hat{\ell}_j) - (\ell_{j+1} - \ell_j) \right|. \quad (11)$$

**PSD-band term.** Let  $f_k = \text{rfftfreq}(L)_k$  denote the normalized real-FFT frequencies. The PSD loss is evaluated only on the band

$$\mathcal{B}_{\text{PSD}} = \{f_k : f_{\min} \leq f_k \leq f_{\max}\}. \quad (12)$$

For a log-amplitude strip  $\ell$ , define

$$P_k(\ell) = |\text{rFFT}(\ell - \bar{\ell})_k|^2, \quad \tilde{P}_k(\ell) = \frac{P_k(\ell)}{\sum_{m \in \mathcal{B}_{\text{PSD}}} P_m(\ell) + \epsilon}. \quad (13)$$

The PSD-band discrepancy is

$$\mathcal{L}_{\text{psd}} = \frac{1}{|\mathcal{B}_{\text{PSD}}|} \sum_{k \in \mathcal{B}_{\text{PSD}}} \left| \tilde{P}_k(\hat{\ell}) - \tilde{P}_k(\ell) \right|. \quad (14)$$

In the experiments,  $[f_{\min}, f_{\max}] = [0.15, 0.50]$  cycles/sample.

**Focus-width term.** The focus-width proxy is computed from the normalized autocorrelation of the centered log-amplitude strip. With zero-padding length  $2L$ ,

$$A_\ell(\tau) = \frac{\mathcal{F}^{-1}(|\mathcal{F}(\ell - \bar{\ell}; 2L)|^2)_\tau}{\mathcal{F}^{-1}(|\mathcal{F}(\ell - \bar{\ell}; 2L)|^2)_0 + \epsilon}. \quad (15)$$

The focus width is the first non-negative lag at which the normalized autocorrelation falls below 0.5,

$$FW(\ell) = \min\{\tau : A_\ell(\tau) < 0.5\}, \quad \mathcal{L}_{\text{fw}} = \frac{|FW(\hat{\ell}) - FW(\ell)|}{FW(\ell) + \epsilon}. \quad (16)$$

This term acts as a compact differentiable proxy for mainlobe broadening in the log-amplitude response.

**Second-order edge term.** The edge term matches the second finite difference of the log-amplitude strip,

$$\mathcal{L}_{\text{edge}} = \frac{1}{L-2} \sum_{j=1}^{L-2} \left| (\hat{\ell}_{j+2} - 2\hat{\ell}_{j+1} + \hat{\ell}_j) - (\ell_{j+2} - 2\ell_{j+1} + \ell_j) \right|. \quad (17)$$

It penalizes mismatched local curvature and suppresses both excessive smoothing and oscillatory ringing.

## A.2 Strip-Informativeness Reweighting

To avoid treating low-structure and high-structure strips identically, each strip in a mini-batch is assigned an informativeness weight. For strip  $i$ , define

$$G_i = \frac{1}{L-1} \sum_{j=1}^{L-1} |\ell_{i,j+1} - \ell_{i,j}|, \quad H_i = \frac{1}{|\mathcal{B}_{\text{PSD}}|} \sum_{k \in \mathcal{B}_{\text{PSD}}} P_k(\ell_i), \quad (18)$$

and

$$I_i = G_i + \frac{1}{2}H_i, \quad \eta_i = \frac{I_i - \min_m I_m}{\max_m I_m - \min_m I_m + \epsilon}. \quad (19)$$

The final per-strip weight is

$$W_i = 0.75 + 0.50 \eta_i, \quad W_i \in [0.75, 1.25]. \quad (20)$$

The batch loss is the mean of the weighted strip losses,

$$\mathcal{L}_{\text{GT}}^{\text{batch}} = \frac{1}{B} \sum_{i=1}^B W_i \mathcal{L}_{\text{GT}}^{(i)}. \quad (21)$$

The PSD band used for both  $H_i$  and  $\mathcal{L}_{\text{psd}}$  is computed from normalized frequencies returned by `torch.fft.rfftfreq`, retaining  $0.15 \leq f \leq 0.50$ .

## A.3 Teacher-Student Distillation Loss

Let  $\hat{z}_s$  be the student prediction,  $\hat{z}_t$  the frozen teacher prediction, and  $z$  the ground-truth target. The student objective combines the ground-truth-aligned focusing loss with a teacher-output distillation penalty,

$$\mathcal{L}_{\text{student}} = \mathcal{L}_{\text{GT}}(\hat{z}_s, z) + \lambda_{\text{KD}} \mathcal{L}_{\text{KD}}(\hat{z}_s, \hat{z}_t). \quad (22)$$

The implemented distillation block is

$$\mathcal{L}_{\text{KD}} = \alpha_c \mathcal{L}_{c,\text{KD}}(\hat{z}_s, \hat{z}_t) + \alpha_\ell \mathcal{L}_{\log}(\hat{z}_s, \hat{z}_t) + \alpha_\rho \mathcal{L}_{\text{ac}}(\hat{z}_s, \hat{z}_t) + \alpha_\phi \mathcal{L}_\phi(\hat{z}_s, \hat{z}_t). \quad (23)$$

Here  $\mathcal{L}_{\log}$  and  $\mathcal{L}_{\text{ac}}$  are evaluated by treating the teacher output as the target in the definitions above. The direct complex-field distillation anchor is implemented as an MSE term,

$$\mathcal{L}_{c,\text{KD}}(\hat{z}_s, \hat{z}_t) = \frac{1}{L} \sum_{j=1}^L |\hat{z}_{s,j} - \hat{z}_{t,j}|^2. \quad (24)$$

This distinguishes the KD anchor from the ground-truth complex term in Eq. (7), which uses the complex magnitude error.

The phase term compares unit complex vectors and weights phase errors by the teacher amplitude:

$$v_s = \frac{\hat{z}_s}{|\hat{z}_s| + \epsilon_\phi}, \quad v_t = \frac{\hat{z}_t}{|\hat{z}_t| + \epsilon_\phi}, \quad (25)$$

$$m_j = \frac{|\hat{z}_{t,j}|^{p_\phi}}{\frac{1}{L} \sum_{m=1}^L |\hat{z}_{t,m}|^{p_\phi} + \epsilon_\phi}, \quad \mathcal{L}_\phi = \frac{\sum_{j=1}^L m_j |v_{s,j} - v_{t,j}|^2}{\sum_{j=1}^L m_j + \epsilon_\phi}. \quad (26)$$

This formulation emphasizes teacher phase where the teacher has non-negligible amplitude and avoids over-weighting phase in near-zero-amplitude regions.

#### A.4 Training Details

**Training–deployment transition.** OSP uses the same learned S4D parameters in two evaluation modes. During training, the student is evaluated in convolutional mode on finite azimuth strips. The S4D convolution kernel is computed with FFT-based zero-padded linear convolution using padding length  $2L$ , and the output is cropped back to the original strip length  $L$ . This avoids circular wrap-around while preserving the causal zero-state boundary condition used by the recurrent processor.

The recurrent representation of S4D layers allows the model to be run in a way such that the output of the current time-step relies only on the current time step and hidden state, allowing for a memory footprint which is independent of the aperture length. We represent each pulse as two real channels, representing real and imaginary parts, and normalize inputs to improve numerical stability. At each step the model produces a complex estimate for the currently resolvable image line.

#### A.5 Training and Evaluation Protocol

Student training uses single-range-bin azimuth strips of length  $L = 1000$ , sampled in row order with `patch_size=[1000,1]` and `stride=[1000,1]`. Each mini-batch contains 61 strips, with gradients accumulated over two mini-batches for an effective batch size of 122. We do not use truncated backpropagation or sequence chunking: each strip is processed as one complete 1000-step sequence. Inputs and targets are normalized with an origin-preserving complex scaling: for each component  $c \in \{\Re, \Im\}$ , both range-compressed inputs and azimuth-compressed targets use  $\tilde{c} = c/2000$ , with inverse transform  $c = 2000\tilde{c}$ . The symmetric bounds  $[-2000, 2000]$  preserve  $0+0i$  exactly. Predictions are inverse-normalized before visualization and before computing all reported metrics. The student is optimized with Adam using betas (0.9, 0.999), initial learning rate  $4 \times 10^{-4}$ , three warm-up epochs, cosine decay, gradient clipping at 0.5, a maximum budget of 300 epochs, and early stopping with patience 40 and `min_delta = 10^{-5}`. The reported student checkpoint is from epoch 57, with saved optimizer learning rate  $10^{-5}$ . Data splitting and patch sampling use seed 42; teacher training additionally fixes the Python, NumPy, PyTorch, and CUDA seeds to 42.

#### A.6 Model architecture details

Table 5: Model architecture hyperparameters for the teacher and student networks.

	Teacher	Student
Number of S4D layers	4	4
Hidden State Size	512	8
Input Dimension	3	3
Position embedding dim.	Range	Range
Initialization	S4D Lin	S4D Lin
Learning Rate	0.0005	0.002

## B Downstream Tasks Details

### B.1 CFAR Vessel Detection

To localize vessel candidates in the focused SAR intensity image we use a two-dimensional cell-averaging constant false alarm rate (CA-CFAR) detector, implemented as a streaming filter that consumes one range line at a time. This matches the line-sequential nature of our front-end and back-end processing pipeline and bounds the detector’s working set to a small number of azimuth lines rather than the full scene.

**Window geometry.** For each cell-under-test (CUT) at position  $(i, j)$  in the intensity image  $x_{i,j} = |s_{i,j}|^2$ , we define two centered square windows: an outer window of side  $2(G + T) + 1$  and an inner (guard) window of side  $2G + 1$ , where  $G$  is the guard half-width and  $T$  is the training half-width. The training set  $\mathcal{T}_{i,j}$  consists of the cells in the outer window that are not in the inner window, so that  $|\mathcal{T}| = N_{\text{train}} = (2(G + T) + 1)^2 - (2G + 1)^2$ . We use  $G = 10$  and  $T = 28$ , giving  $N_{\text{train}} = 5,776$  training cells.

**Detection rule.** Under the standard assumption that homogeneous clutter intensity follows an exponential distribution, the maximum-likelihood noise estimate is the training-cell mean  $\hat{\mu}_{i,j} = \frac{1}{N_{\text{train}}} \sum_{(p,q) \in \mathcal{T}_{i,j}} x_{p,q}$ , and the CA-CFAR decision compares the CUT to a scaled version of this estimate,

$$x_{i,j} \geq \alpha \hat{\mu}_{i,j}, \quad \alpha = N_{\text{train}} \left( P_{\text{fa}}^{-1/N_{\text{train}}} - 1 \right), \quad (27)$$

where the multiplier  $\alpha$  is chosen so that the per-cell probability of false alarm is  $P_{\text{fa}}$  in the exponential-clutter model. We target  $P_{\text{fa}} = 10^{-6}$ .

**Streaming computation.** A naive implementation evaluates a 2D sum over  $\mathcal{T}_{i,j}$  at every pixel. We instead exploit the separability of the box sums. For each range bin  $j$ , we maintain two running azimuth-column sums,  $C_j^{\text{outer}}$  over the most recent  $2(G + T) + 1$  lines and  $C_j^{\text{inner}}$  over the central  $2G + 1$  lines centered on the CUT line. Once a CUT line has  $G + T$  lines of azimuth context above and below it, the 2D outer and inner box sums for every range bin on that line are obtained in a single 1D pass along range by applying a length  $2(G + T) + 1$  and a length  $2G + 1$  box filter, respectively, to the column-sum vectors. The training sum is then the difference of these two box sums, yielding the per-pixel noise estimate  $\hat{\mu}_{i,j}$  and threshold for the entire CUT line at constant cost per pixel and constant memory in azimuth. The detector emits decisions with a fixed latency of  $G + T = 38$  azimuth lines relative to the input stream.

**Boundary handling.** At the leading and trailing edges of the swath the outer window extends beyond the available data. We use reflect padding in azimuth, mirroring buffered lines about the first and last real lines, which is consistent with the boundary mode of standard uniform-filter implementations and avoids the bias that zero-padding would introduce into the noise estimate.

**Post-processing.** The binary detection map is post-filtered by removing connected components smaller than  $K_{\text{min}} = 3$  pixels to suppress isolated single-pixel detections that are dominated by speckle rather than persistent scatterers. The resulting mask is the set of vessel candidates passed to downstream evaluation

### B.2 Rapid Flood Detection

To obtain a binary water mask from a focused single-look complex SAR scene, we exploit the fact that calm water surfaces behave as near-specular reflectors at C-band: incident energy is reflected away from the sensor in the forward direction, so water pixels return very little backscattered power and appear as dark regions in intensity imagery. Land surfaces, by contrast, scatter diffusely and yield substantially higher returns. A simple intensity threshold therefore suffices to separate the two classes.

**Intensity formation.** Given the complex-valued focused image  $z \in \mathbb{C}^{H \times W}$ , we form the per-pixel radar intensity

$$I(x, y) = |z(x, y)|^2, \quad (28)$$

which is proportional to the radar cross-section of the resolution cell (up to the system calibration constant, which we do not require).

**Smoothing.** In order to lower the impact of noise on the output of the segmentation map we convolve the intensity image with a  $K \times K$  spatial kernel,

$$\tilde{I}(x, y) = (h_K * I)(x, y), \quad (29)$$

where  $h_K$  is either a uniform (boxcar) filter of side length  $K$ .

**Thresholding.** A pixel is labelled as water when its normalised intensity falls below a fixed cutoff  $\tau$ ,

$$M(x, y) = \mathbf{1}[I_{\text{dB}}(x, y) < \tau], \quad (30)$$

with  $\tau = -9$  dB chosen empirically.

**Connected-component cleanup.** Scans produced with OSP or traditional methods tend to have noise present. As such, to minimize the impact of random noise on the quality of our segmentation map, we label the binary mask under 8-connectivity and discard every connected component whose area is smaller than  $A_{\text{min}} = 600$  pixels, retaining only contiguous water bodies of physically plausible size. The final mask is

$$M^*(x, y) = \mathbf{1}[(x, y) \in \mathcal{C}_i, |\mathcal{C}_i| \geq A_{\text{min}}], \quad (31)$$

where  $\{\mathcal{C}_i\}$  are the connected components of  $M$ . The resulting binary map  $M^*$  is used as a weak label for downstream evaluation; the pipeline is fully unsupervised and deterministic, requiring only the focused complex image as input.

**Limitations** The implementation of our code for this downstream tasks was not strictly a linewise implementation, however in principle this task could be implemented in a linewise manner. If the connected-component cleanup step is removed, all other steps could be implemented on a small rolling buffer of a few azimuth lines.

## C Computational Complexity Derivations

In this appendix we present a computational complexity derivation for two baseline range-doppler algorithm implementations, as well our Online Processor, as below:

- Batched RDA
- Linewise RDA
- Online Processor

In the computational complexity derivations below we make the following assumptions: Let  $N_a$  and  $N_r$  denote the number of azimuth (slow-time) and range (fast-time) samples, respectively, so that the raw phase-history data occupies an  $N_a \times N_r$  complex-valued matrix. In all three algorithms, the range compression, range-cell migration correction (RCMC), and azimuth compression kernels, where used, are precomputed before data acquisition begins and therefore we do not count them as contributing to the run-time complexity counts reported here. It should be noted, within this appendix we consider operations in terms of complex operations. All FFT computations in this appendix are assumed to be using the standard radix-2 Cooley-Tukey FFT.

### C.1 Batched Range-Doppler Algorithm

The standard RDA processes the entire  $N_a \times N_r$  phase-history array in one pass - we refer to this as the "batched" RDA as it focuses SAR data in batches. Its stages proceed as follows.

**Step 1: Range Compression** First, each of the  $N_a$  azimuth lines is independently transformed to the range-frequency domain. Following this, each of the  $N_r$  range lines is also independently transformed to the azimuth frequency domain, yielding the full two-dimensional frequency representation of the scene. Finally, the precomputed range matched filter  $H_r$  is applied via element-wise complex multiplication across the  $N_a \times N_r$  grid.

**Step 2: Range-Cell Migration Correction** In the two-dimensional frequency domain, each sample undergoes a range shift correction by means of an elementwise multiplication with an RCMC kernel,  $H_{rcmc}$ , requiring a single complex multiply-accumulate operation per cell.

**Step 3: Azimuth Compression** Following RCMC, an inverse FFT is applied along the range direction to return each azimuth line to the range-time domain, producing the Range-Doppler representation. The precomputed azimuth matched filter  $H_a$  is then applied via elementwise complex multiplication in the Range-Doppler domain. Finally, an inverse FFT along the azimuth direction recovers the focused complex image.

We find that the total computational complexity of this algorithm in terms of  $N_a$  and  $N_r$  is  $N_a N_r [2 \log_2(N_a N_r) + 3]$ , giving an order of  $\mathcal{O}(N_a N_r \log(N_a N_r))$ . We present a breakdown of the computational cost of each stage in Table 6

Table 6: Per-stage operation count for the Range-Doppler Algorithm with precomputed filters.

Step	Stage	Operation	Cost
1	Range FFT	$N_a$ FFTs of length $N_r$	$N_a N_r \log_2 N_r$
2	Azimuth FFT	$N_r$ FFTs of length $N_a$	$N_a N_r \log_2 N_a$
3	Range compression	Element-wise $\odot H_r$	$N_a N_r$
4	RCMC	Element-wise $\odot H_{RCMC}$	$3 \cdot N_a N_r$
5	Range IFFT	$N_a$ IFFTs of length $N_r$	$N_a N_r \log_2 N_r$
6	Azimuth compression	Element-wise $\odot H_a$	$N_a N_r$
7	Azimuth IFFT	$N_r$ IFFTs of length $N_a$	$N_a N_r \log_2 N_a$
<b>Total</b>			$N_a N_r [2 \log_2(N_a N_r) + 3]$
<b>Order</b>			$\mathcal{O}(N_a N_r \log(N_a N_r))$

### Line-wise Range-Doppler Algorithm

The batched RDA requires all  $N_a$  range lines to be resident in memory simultaneously, since the azimuth FFT must span the full synthetic aperture (on the order of tens of thousands of pulses for Sentinel-1 stripmap data). A line-wise variant is possible, but not commonly used, and can be implemented if a certain amount of phase history is buffered; while this is impractical in most real systems, we include it here to provide a direct algorithmic baseline against which to compare our proposed method.

In such a method we maintain a rolling buffer of  $N_b$  range lines simultaneously. The reason for doing this is that after the RC and RCMC step, depending on the squint angle, SAR information in the sample under processing is spread across many azimuth time steps. As such, to focus properly any given azimuth cell, it is required to have knowledge of the data corresponding to the time steps before and after this cell's occurrence. This value is related to the length of the synthetic aperture,  $L_{sa}$ :

$$L_{sa} = R_o \cdot \Theta \quad (32)$$

where  $\Theta$  is the angular span of the SAR antenna and  $R_o$  is the range of closest approach. Following this, we can approximate  $\Theta$  as the ratio of the transmitted wavelength  $\mu$  and the physical antenna length:

$$L_{ant} : \Theta \approx \frac{\mu}{L_{ant}} \quad (33)$$

Finally, given that:

$$N_{az} = \frac{L_{SA}}{\Delta x_{az}} \quad (34)$$

where  $\Delta x_{az}$  is the ground-projected size, we can obtain:

$$N_{az} \approx \frac{R_o \mu}{L_{ant} \Delta x_{az}} \quad (35)$$

resulting in an estimate of approximately 486 azimuth cells using Sentinel-1 characteristics. As such, we use a buffer of 486 cells looking forward and backward, resulting in a buffer of  $N_b = 972$ .

We assume this number for our computational complexity assumptions, however it should be noted that  $R_0$  changes for different stripmap modes, and we present these values below in Table 7 for the reader’s reference.

Table 7: Near-range slant range  $R_0$  for Sentinel-1 stripmap beams at minimum orbit altitude ( $\sim 698$  km). These values contextualize the buffer-size estimate used in the linewise-RDA latency and complexity calculations.

Beam	Off-nadir angle [°]	Incidence angle [°]	$R_0$ [km]
S1	17.93	19.99	737.9
S2	21.00	23.45	753.8
S3	26.18	29.33	788.4
S4	30.87	34.71	829.8
S5	35.07	39.62	877.2
S6	37.53	42.53	910.6

It should be noted that the total delay for such an implementation is equal to the processing latency summed with a buffering latency. The buffering latency is associated with the time it takes for the satellite to fill the buffer of phase history in the forward direction after the data for the range line of interest has been recorded but before the data associated with the range line of interest can start to be processed. For a SAR system with a sampling frequency of 2000Hz, this delay is around 0.246 seconds, as such we include this in our latency calculations.

**Per-output-line computation cost.** This formulation would use a sliding buffer of the most recent  $N_b$  range-compressed pulses. Each time a new slow-time sample arrives, the following operations are performed:

**Step 1: Range Compression** Each of the  $N_b$  range lines in the buffer are independently transformed to the range-frequency domain. However, this action only has to occur once per range-line, and after performed the results for this can be cached, such that for each timestep only the most recent range line needs to be converted to the range-frequency domain. Following this, each of the  $N_r$  range bins are independently transformed to the azimuth-frequency domain, yielding a two-dimensional frequency representation  $N_b$  slow-time timesteps of phase history. Next, the precomputed range matched filter  $H_r$  is applied via element-wise complex multiplication across the  $N_b \times N_r$  grid.

**Step 2: Range-Cell Migration Correction** In the two-dimensional frequency domain, each sample undergoes a range shift that is corrected via elementwise multiplication with  $H_{rcmc}$

**Step 3: Azimuth Compression** Following RCMC, an inverse FFT is applied along the range direction to return each azimuth line to the range-time domain, producing the Range-Doppler representation. A final inverse FFT along azimuth recovers a partially focused complex image

**Step 4: Extract Valid Data** Only one range row of data is valid and can be considered fully focused from the buffer output. Thus, we extract one valid range row of focused SAR data from the center of the output image and disregard the remaining data. Then, the previous steps are repeated every PRI, assuming  $N_a$  pulses across the entire sample, this results in a total complexity of  $N_r [\log_2 N_r + N_b [3 + 2 \log_2 N_r + \log_2 N_b]]$ . A detailed breakdown of the computational complexity of each step is presented in Table 8

### Line-wise State-Space Model

Our proposed Online Processor uses an SSM operating in the recurrent mode: it maintains a hidden state per range cell that persists in dimension across slow-time steps. Each new pulse is range-compressed and the resulting  $N_r$  range-cell values are fed into SSM instances with independent hidden states, which implicitly learn azimuth compression and RCMC without any explicit FFT along the azimuth direction. The SSM has fixed architecture parameters:  $K$  layers, hidden dimension  $H$ , and channel number  $N$ . In our model we also use fully-connected layers, at the front and end of the model and within the S4D layers. The 1st fully connected layer requires 8 multiply accumulates

Table 8: Per-stage operation count for the Line-wise Range-Doppler Algorithm. Each block of operations is executed once per incoming pulse and repeated  $N_a$  times.  $N_b$  is the rolling buffer size (constant for a given SAR mode).

Step	Stage	Operation	Cost (per pulse)
1	Range FFT	single FFT of length $N_r$	$N_r \log_2 N_r$
2	Azimuth FFT	$N_r$ FFTs of length $N_b$	$N_b N_r \log_2 N_b$
3	Range compression	Element-wise $\odot H_r$	$N_b N_r$
4	RCCM	Element-wise $\odot H_{RCCM}$	$N_b N_r$
5	Range IFFT	$N_b$ IFFTs of length $N_r$	$N_b N_r \log_2 N_r$
6	Azimuth compression	Element-wise $\odot H_a$	$N_b N_r$
7	Azimuth IFFT	$N_r$ IFFTs of length $N_b$	$N_b N_r \log_2 N_b$
<b>Per-pulse total</b>			$N_r [\log_2 N_r + N_b [3 + 2 \log_2 N_r + \log_2 N_b]]$
<b>Full-scene total</b>		$\times N_a$ pulses	$N_a N_r [\log_2 N_r + N_b [3 + 2 \log_2 N_r + \log_2 N_b]]$
<b>Order</b>			$\mathcal{O}(N_a N_r N_b \log(N_b N_r))$

and the other layers all require 4 multiply accumulates. As such, we will represent this fixed number of MACs per model inference as  $X$ . Given that the architecture of the model is fixed, our online processor only increases in algorithmic complexity in terms of the number of range bins  $N_r$  and the number of slow-time steps  $N_a$ . However, we note that at smaller values of  $N_r$  and  $N_a$  that  $X$  will be significant.

**Step 1: Range Compression** Perform one FFT of length  $N_r$  on input range line. Then apply the precomputed matched filter by means of an elementwise multiply. Finally, return to range-time domain by performing IFFT of length  $N_r$  on the range line

**Step 2: SSM inference** We perform one neural network forward pass of our tiny model per range cell. We denote the inference cost of the tiny neural network as  $X$  MACs - constant with respect to both  $N_a$  and  $N_r$  - so performing across  $N_r$  range cells each timesteps results in computational complexity of  $X \times N_r$ .

As such, our total computational complexity comes out to  $N_a N_r [1 + X + 2 \log_2 N_r]$ .

Table 9: Per-stage operation count for the Online Processor. Each block of operations is executed once per incoming pulse and repeated  $N_a$  times.

Step	Stage	Operation	Cost (per pulse)
1	Range FFT	single FFT of length $N_r$	$N_r \log_2 N_r$
2	Range compression	Element-wise $\odot H_r$	$N_r$
3	Range IFFT	$N_b$ IFFTs of length $N_r$	$N_r \log_2 N_r$
4	Model Inference	$N_r$ model inferences	$X N_r$
<b>Per-pulse total</b>			$N_r [1 + X + 2 \log_2 N_r]$
<b>Full-scene total</b>		$\times N_a$ pulses	$N_a N_r [1 + X + 2 \log_2 N_r]$
<b>Order</b>			$\mathcal{O}(N_a N_r \log(N_r))$

It should be noted that for the version of our algorithm used in the experiments presented in this paper, the operations of  $X$  is larger than  $\log_2 N_r$ , however since  $X$  is of a fixed size, as the data size of the SAR scan increases (portending the increase of  $N_r$  and  $N_a$ ), this scales as  $\mathcal{O}(N_a N_r \log_2 N_r)$ , which is particularly pertinent given the trend of SAR systems to larger and larger data volumes. In Table 10 we summarize the results of our computational complexity analysis.

## D Computational Cost Analysis

This appendix derives the floating-point operation (FLOP) counts for our two SAR processing benchmarks and our proposed online processor. For this comparison, we assume all three algorithms process a complex-valued SAR data matrix of size  $N_a \times N_r = 20,000 \times 20,000$ . This close to the

Table 10: Summary of total computational cost across methods.

Method	Per-pulse total	Full-scene total
Batched RDA	–	$N_a N_r [2 \log_2(N_a N_r) + 3]$
Line-wise RDA	$N_r [\log_2 N_r + N_b [3 + 2 \log_2 N_r + \log_2 N_b]]$	$N_a N_r [\log_2 N_r + N_b [3 + 2 \log_2 N_r + \log_2 N_b]]$
Line-wise SSM	$N_r (2 \log_2 N_r + 1 + X)$	$N_a N_r (2 \log_2 N_r + 1 + X)$

size of a typical Sentinel-1 stripmap scan, although they tend to be long along the azimuth direction. The linewise algorithms process one azimuth line at a time and are therefore applied  $N_a = 20,000$  times to fully process the entire scan.

### D.1 Counting Conventions

Throughout this appendix, each real-valued multiplication or addition is counted as one FLOP. By extension, a complex–complex multiplication  $(a + bi)(c + di) = (ac - bd) + (ad + bc)i$  requires 4 real multiplies and 2 real adds = 6 FLOPs. A complex–real multiplication  $(a + bi) \cdot c = ac + bci$  requires 2 real multiplies = 2 FLOPs. A complex addition requires 2 real adds = 2 FLOPs. A radix-2 complex FFT of length  $N$  requires approximately  $5N \log_2 N$  real FLOPs (following [27]). All tensors use `complex64` (8 bytes per element: `2 × float32`).

### D.2 Batched RDA

A single iteration processes the full  $20,000 \times 20,000$  complex matrix. The total steps are as follows:

1. Row-wise FFT, Column-wise FFT
2. Three element-wise complex multiplies (RC, RCMC, AC filters)
3. Row-wise IFFT, Column-wise IFFT

#### D.2.1 FLOPs

Table 11: FLOP breakdown for batched RDA ( $20,000 \times 20,000$ ).

Operation	Expression	GFLOPs
FFT dim=1	$20,000 \times 5 \times 20,000 \times \log_2(20,000)$	28.6
FFT dim=0	$20,000 \times 5 \times 20,000 \times \log_2(20,000)$	28.6
Multiply (RC)	$20,000^2 \times 6$	2.4
Multiply (RCMC)	$20,000^2 \times 6$	2.4
Multiply (AC)	$20,000^2 \times 6$	2.4
IFFT dim=1	(same as FFT dim=1)	28.6
IFFT dim=0	(same as FFT dim=0)	28.6
<b>Total</b>		<b>121.6</b>

### D.3 Linewise RDA

Here we also assume a buffer length  $N_b$  of 972 as in Appendix C Each iteration operates on a  $972 \times 20,000$  complex matrix and performs:

1. Row-wise FFT (dim=1,  $N = 20,000$ , applied to 1 rows)
2. Column-wise FFT (dim=0,  $N = 972$ , applied to 20,000 columns)
3. Element-wise complex multiply with range-compression filter
4. Element-wise complex multiply with range-cell-migration-correction filter
5. Element-wise complex multiply with azimuth-compression filter
6. Row-wise IFFT (dim=1,  $N = 20,000$ , applied to 972 rows)
7. Column-wise IFFT (same cost as step 2)

Table 12: FLOP breakdown per linewise RDA iteration ( $972 \times 20,000$ ).

Operation	Expression	GFLOPs
FFT dim=1	$5 \times 20,000 \times \log_2(20,000)$	0.000143
FFT dim=0	$20,000 \times 5 \times 972 \times \log_2(972)$	0.965
Multiply (RC filter)	$972 \times 20,000 \times 6$	0.0194
Multiply (RCMC filter)	$972 \times 20,000 \times 6$	0.0194
Multiply (AC filter)	$972 \times 20,000 \times 6$	0.0194
IFFT dim=1	$972 \times 20,000 \times \log_2(20,000)$	0.277
IFFT dim=0	(same as FFT dim=0)	0.965
<b>Per-iteration total</b>		<b>2.27</b>
<b>Per-scan total</b>	$: \times 20,000$	<b>45400</b>

### D.3.1 FLOPs Per Iteration

### D.4 Online Processor

Each iteration operates on one range line ( $1 \times 20,000$  complex) and performs:

1. Row-wise FFT, complex multiply with RC filter, row-wise IFFT (range compression)
2. Tiny Neural network forward pass on all  $N_r = 20,000$  range cells

This process is then repeated in a linewise manner on each input range line of raw SAR data.

The Tiny Model consists of the following layers, applied sequentially:

fc1  $\rightarrow$  ssm2  $\rightarrow$  act  $\rightarrow$  fc3  $\rightarrow$  ssm4  $\rightarrow$  act  $\rightarrow$  fc5  $\rightarrow$  ssm6  $\rightarrow$  act  $\rightarrow$  fc7  $\rightarrow$  ssm8  $\rightarrow$  act  $\rightarrow$  fc9  
 $\rightarrow$  fc10

Table 13: Online Processor FLOPs estimate.

Operation	Expression	FLOPs per Cell	MFLOPs per line
FFT dim=1	$1 \times 5 \times 20,000 \times \log_2(20,000)$		1.43
Multiply (RC filter)	$20,000 \times 6$		0.12
IFFT dim=1	(same as FFT)		1.43
<b>Front End Per-iteration total</b>			<b>2.98</b>
fc1	FC input	18	
ssm2	S4D	146	
act	LeakyReLU	2	
fc3	FC	10	
ssm4	S4D	146	
act	LeakyReLU	2	
fc5	FC	10	
ssm6	S4D	146	
act	LeakyReLU	2	
fc7	FC	10	
ssm8	S4D	146	
act	LeakyReLU	2	
fc9	FC	10	
fc10	FC	10	
<b>Tiny Model Total</b>		<b>660</b>	<b>13.2</b>
<b>Online Processor Total</b>			<b>16.18</b>
<b>Online Processor Per Scan Total</b>			<b>323600</b>

## E Memory Footprint Calculations

### E.1 Batched RDA

Four tensors ( $x$ ,  $rc\_filter$ ,  $rcmc\_filter$ ,  $ac\_filter$ ), each  $20,000 \times 20,000 \times 8 = 3.2$  GB, plus an FFT scratch buffer:

$$M_{RDA, batch} \approx 5 \times 3.2 = 16 \text{ GB (peak)} \tag{36}$$

#### E.1.1 Linewise RDA

Each of the four tensors ( $x$ ,  $rc\_filter$ ,  $ac\_filter$ ) occupies  $972 \times 20,000 \times 8 = 156$  MB. Including a scratch buffer for the in-place FFT:

$$M_{RDA, line} \approx 5 \times 156 = 780 \text{ MB (peak)} \tag{37}$$

#### E.1.2 Online Processor

Table 14: Memory breakdown for linewise SSM.

Component	Expression	Size
Signal tensors ( $x$ , $rc\_filter$ )	$2 \times 20,000 \times 8$	320 KB
SSM state (4 layers $\times N_r \times [2, 4]$ complex)	$4 \times 20,000 \times 2 \times 4 \times 8$	5.12 MB
Model parameters (real and complex)	$96 \times 8 + 48 \times 4$	<1 KB
Embedding tensor ( $N_r \times 4$ , real)	$20,000 \times 4 \times 4$	320 KB
<b>Total</b>		<b><math>\approx 5.8</math> MB</b>

## F Dataset

The dataset on which our model was trained used a training-validation-testing split, with each of the splits being in geographically independent locations with both land and sea data to demonstrate the generalizability of our model. This dataset also included samples from all 6 stripmap modes used by the sentinel-1 satellites. We also present a map showing the geographical spread of our samples in figure 6

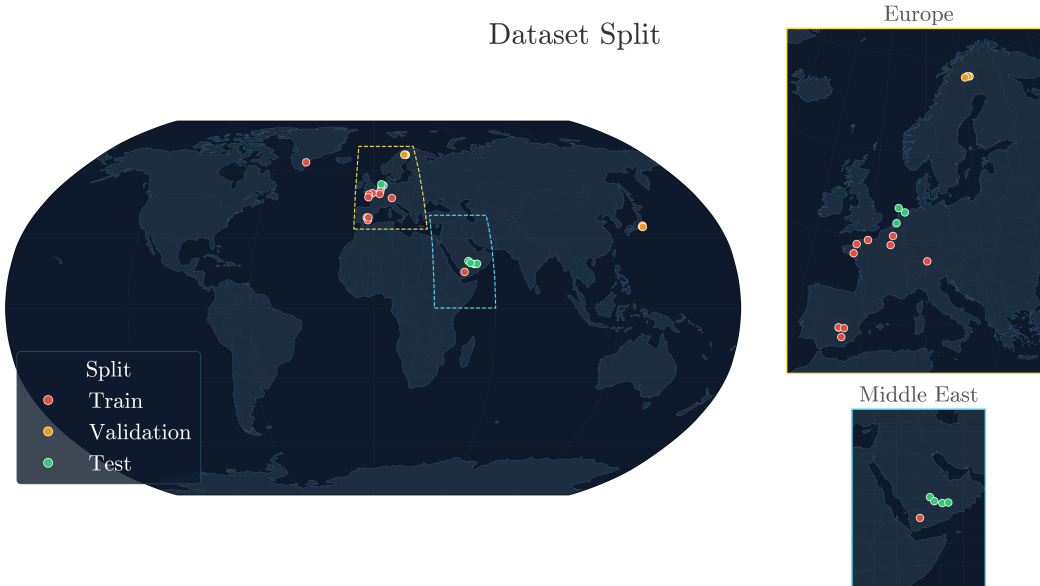


Figure 6: Maya4 subset scan locations map.

Table 15: Dataset split into training, validation, and test scenes.

Split	Filename	
Train	s1c-s1-raw-s-vv-20250417t025744-20250417t025817-001927-003c59.zarr	
	s1c-s1-raw-s-vv-20250417t025809-20250417t025828-001927-003c59.zarr	
	s1c-s2-raw-s-vv-20250403t062508-20250403t062540-001725-002fa3.zarr	
	s1c-s2-raw-s-vv-20250405t060531-20250405t060604-001754-00317b.zarr	
	s1c-s2-raw-s-vv-20250405t060556-20250405t060629-001754-00317b.zarr	
	s1c-s2-raw-s-vv-20250427t062507-20250427t062539-002075-004519.zarr	
	s1c-s4-raw-s-vv-20250329t061359-20250329t061431-001652-002b01.zarr	
	s1c-s4-raw-s-vv-20250329t061424-20250329t061459-001652-002b01.zarr	
	s1c-s4-raw-s-vv-20250417t091925-20250417t091957-001931-003c9c.zarr	
	s1c-s4-raw-s-vv-20250417t091950-20250417t092006-001931-003c9c.zarr	
	s1c-s5-raw-s-vv-20250416t052542-20250416t052609-001914-003b87.zarr	
	s1c-s6-raw-s-vv-20250405t060936-20250405t060953-001754-00317f.zarr	
	s1c-s6-raw-s-vv-20250422t061414-20250422t061446-002002-0040d4.zarr	
	s1c-s6-raw-s-vv-20250422t061439-20250422t061511-002002-0040d4.zarr	
	s1c-s6-raw-s-vv-20250422t061504-20250422t061520-002002-0040d4.zarr	
	s1c-s6-raw-s-vv-20250429t060847-20250429t060920-002104-0046e6.zarr	
	Validation	s1c-s1-raw-s-vv-20250328t052810-20250328t052835-001637-002a0d.zarr
		s1c-s2-raw-s-vv-20250331t205042-20250331t205107-001690-002d5c.zarr
s1c-s3-raw-s-vv-20250414t083258-20250414t083323-001887-0039f0.zarr		
s1c-s4-raw-s-vv-20250330t051150-20250330t051214-001666-002bd3.zarr		
s1c-s4-raw-s-vv-20250407t204234-20250407t204258-001792-0033e2.zarr		
s1c-s5-raw-s-vv-20250406t050339-20250406t050403-001768-003264.zarr		
Test	s1c-s5-raw-s-vv-20250420t160613-20250420t160637-001979-003f6e.zarr	
	s1c-s6-raw-s-vv-20250401t161424-20250401t161448-001702-002e19.zarr	
	s1c-s1-raw-s-vv-20250424t170801-20250424t170839-002038-0042df.zarr	
	s1c-s2-raw-s-vv-20250405t060506-20250405t060539-001754-00317b.zarr	
	s1c-s4-raw-s-vv-20250328t145502-20250328t145535-001643-002a6d.zarr	
	s1c-s4-raw-s-vv-20250328t145527-20250328t145555-001643-002a6d.zarr	
	s1c-s4-raw-s-vv-20250422t172412-20250422t172445-002009-00413d.zarr	
	s1c-s4-raw-s-vv-20250426t023204-20250426t023237-002058-004414.zarr	
s1c-s5-raw-s-vv-20250421t022419-20250421t022447-001985-003fc0.zarr		
s1c-s5-raw-s-vv-20250421t145445-20250421t145518-001993-004045.zarr		

## G Extended Discussion

### G.1 Interpretation

The central result of this paper is that, after standard front-end preprocessing, a substantial portion of the azimuth-focusing operator can be represented as a compact causal dynamical system. This explains why OSP can reduce latency and memory so aggressively without collapsing reconstruction quality: the model does not try to learn all of SAR imaging end to end, but instead targets the specific long-range phase-history transformation that remains after range-domain preparation.

The experiments also clarify which design choices matter most. Performance improvements did not come primarily from making the teacher wider or deeper; rather, they came from regularization and from balancing losses that preserve amplitude structure, sharpness, and spectral content. This is consistent with the intuition that online focusing is less a brute-force function-approximation problem than a structurally constrained operator-learning problem.

### G.2 Complexity and FLOP estimates

To highlight the advantages of our Online Processor, we compare our proposed method against two implementations of the RDA algorithm, one being the commonly used "batched" RDA where all operations are performed in batches, and the other is a version of the RDA which relies on buffering a window of SAR history that can perform focusing of a single range line at a time that we call the linewise RDA. We calculate that to be able to make an accurate focusing of a single line of SAR data, the linewise RDA must maintain a rolling buffer of 972 range lines, i.e. 486 range lines ahead of the line of interest and 486 lines behind the line of interest.

For our computational complexity estimation we assume that the values for RC, RCMC and AC filters are calculated prior to the beginning of the SAR data collection and thus ignore these contributions to computational cost. The reason for this is in the application of live SAR focusing we care only about computational cost which occurs between the points of collecting raw data and outputting focused data that contributes to the delay in obtaining focused data.

Table 16: Complexity, latency, memory, and compute comparison. Lower latency, memory, and GFLOPs per row are better.

Method	Complexity	Single-line latency (ms)*	Full scan latency (ms)*	Memory footprint	GFLOPs per scan	GFLOPs per row
Traditional RDA	$\mathcal{O}(N_a N_r \log(N_a N_r))$	N/A <sup>†</sup>	<b>27,444</b>	16 GB	<b>122</b>	N/A <sup>†</sup>
Linewise RDA	$\mathcal{O}(N_a N_r N_b \log(N_b N_r))$	857 (+243) <sup>‡</sup>	17,140,000	780 MB	45,400	2.27
<i>This work</i>	$\mathcal{O}(N_a N_r \log(N_r))$	<b>15.1</b>	302,000	<b>6 MB</b>	324	<b>0.016</b>

\*Latency measured on a single core of an AMD EPYC 7343 CPU.

<sup>†</sup>Cannot be used to process individual range lines in an online manner.

<sup>‡</sup>Processing starts only after the history buffer is filled, adding delay beyond pure compute time.

Due to the fact our model uses fixed memory footprint SSM layers as its backbone and does not require buffering data in the azimuth direction, we obtain a far superior memory footprint to both baselines. Our online formulation enables drastically reduced data-in-to-data-out focusing latency; however, accumulated over an entire scan, the computational complexity of our technique is worse and that is also reflected in full scan processing latency. We show detailed computational complexity and FLOPs derivations in Appendices C and D.

### G.3 Limitations and failure cases

Our study is intentionally narrow in operating regime. The current formulation assumes a linear synthetic aperture: stripmap acquisition, broadside geometry, modest angular extent, and front-end preprocessing that already makes the azimuth task well conditioned. The deployed model is therefore not yet a drop-in replacement for wide-squint, spotlight, or heavily motion-corrupted collections.

Failure cases are most likely when those assumptions are violated. Large residual motion errors, stronger-than-expected range migration, unseen PRF or bandwidth regimes, and scene statistics far from Maya4 can all cause defocus, amplitude bias, or temporal lag in the emitted rows. In addition, because OSP is causal, it cannot exploit arbitrarily large future context in the way a fully offline batch imager can, so some loss of fidelity relative to the best offline methods should be expected in challenging scenes.

### G.4 Operational considerations

Operational SAR focusing in real systems typically requires motion compensation (IMU/GNSS + residual corrections), sidelobe control (windowing, multi-looking), and radiometric/geometric calibration. Residual phase errors (platform motion, atmosphere/ionosphere, uncompensated squint) are commonly addressed with robust data-driven autofocus, with PGA remaining a strong baseline in many pipelines [28, 2]. These considerations highlight why deployment constraints matter for the proposed method. In practice, the value of online focusing is not only reduced FLOPs, but the ability to move interpretable image evidence earlier in the decision loop. A processor that emits focused rows incrementally allows downstream modules such as CFAR detection, target cueing, or adaptive mode selection to begin operating before a full aperture has been collected.

At the same time, OSP should be viewed as one component in a larger operational chain rather than as a complete replacement for classical estimation machinery. Motion compensation, autofocus, calibration, and uncertainty monitoring remain necessary, and in high-assurance settings the online product may be best used for rapid triage while slower high-fidelity imaging produces archival outputs.

### G.5 Sensitivity and robustness

The teacher sweeps suggest that the method is more sensitive to objective design than to raw model size. Moderate changes to dropout and to the amplitude-correlation/edge balance produced larger

gains than simply increasing capacity, and the final frontier showed a meaningful trade-off between balanced structural fidelity (ridge family) and RMSE specialization (selectivity family). This is encouraging for deployment because it suggests that good operating points can be found without dramatically increasing compute.

Robustness, however, is not fully characterized by the current experiments. The present study uses a single benchmark family and configuration sweeps rather than repeated-seed uncertainty estimates or explicit domain-shift stress tests. A stronger robustness claim would require evaluation across broader sensing conditions, perturbations of acquisition parameters, and downstream closed-loop tasks in which latency, not only image similarity, is measured directly.

## NeurIPS Paper Checklist

### 1. Claims

Question: Do the main claims made in the abstract and introduction accurately reflect the paper’s contributions and scope?

Answer: [Yes]

Justification: We believe that our paper provides evidence to support the claims we make in our introduction, and we provide extra evidence to support this in our appendices as well. We believe our abstract accurately summarizes our paper and the claims we make in it, regarding our novel algorithmic formulation and the performance of our trained focusing models

Guidelines:

- The answer [Yes] means that the abstract and introduction do not include the claims made in the paper.
- The abstract and/or introduction should clearly state the claims made, including the contributions made in the paper and important assumptions and limitations. A [No] or [N/A] answer to this question will not be perceived well by the reviewers.
- The claims made should match theoretical and experimental results, and reflect how much the results can be expected to generalize to other settings.
- It is fine to include aspirational goals as motivation as long as it is clear that these goals are not attained by the paper.

### 2. Limitations

Question: Does the paper discuss the limitations of the work performed by the authors?

Answer: [Yes]

Justification: We mention the limitations of our work in the main text of our paper and include our assumptions. We also provide further discussion of limitations in the appendices. We outline limitations such our method has currently only been shown to work for stripmap mode SAR acquisitions that assume minimal range cell migration, and we draw attention to the fact that focusing quality of our student model is not as strong as our teacher model or as traditional digital signal processing based techniques. We ensure as much as possible within the page limit to outline any important assumptions made by our experiments in the main text, and where there is not space to do so we put our assumptions in appendices for reference. We discuss how the computational efficiency of our method scales with the data size of SAR samples being processed.

Guidelines:

- The answer [N/A] means that the paper has no limitation while the answer [No] means that the paper has limitations, but those are not discussed in the paper.
- The authors are encouraged to create a separate “Limitations” section in their paper.
- The paper should point out any strong assumptions and how robust the results are to violations of these assumptions (e.g., independence assumptions, noiseless settings, model well-specification, asymptotic approximations only holding locally). The authors should reflect on how these assumptions might be violated in practice and what the implications would be.

- The authors should reflect on the scope of the claims made, e.g., if the approach was only tested on a few datasets or with a few runs. In general, empirical results often depend on implicit assumptions, which should be articulated.
- The authors should reflect on the factors that influence the performance of the approach. For example, a facial recognition algorithm may perform poorly when image resolution is low or images are taken in low lighting. Or a speech-to-text system might not be used reliably to provide closed captions for online lectures because it fails to handle technical jargon.
- The authors should discuss the computational efficiency of the proposed algorithms and how they scale with dataset size.
- If applicable, the authors should discuss possible limitations of their approach to address problems of privacy and fairness.
- While the authors might fear that complete honesty about limitations might be used by reviewers as grounds for rejection, a worse outcome might be that reviewers discover limitations that aren't acknowledged in the paper. The authors should use their best judgment and recognize that individual actions in favor of transparency play an important role in developing norms that preserve the integrity of the community. Reviewers will be specifically instructed to not penalize honesty concerning limitations.

### 3. Theory assumptions and proofs

Question: For each theoretical result, does the paper provide the full set of assumptions and a complete (and correct) proof?

Answer: [Yes]

Justification: We provide full assumptions and mathematical derivation for our computational complexity analyses in our appendices.

Guidelines:

- The answer [N/A] means that the paper does not include theoretical results.
- All the theorems, formulas, and proofs in the paper should be numbered and cross-referenced.
- All assumptions should be clearly stated or referenced in the statement of any theorems.
- The proofs can either appear in the main paper or the supplemental material, but if they appear in the supplemental material, the authors are encouraged to provide a short proof sketch to provide intuition.
- Inversely, any informal proof provided in the core of the paper should be complemented by formal proofs provided in appendix or supplemental material.
- Theorems and Lemmas that the proof relies upon should be properly referenced.

### 4. Experimental result reproducibility

Question: Does the paper fully disclose all the information needed to reproduce the main experimental results of the paper to the extent that it affects the main claims and/or conclusions of the paper (regardless of whether the code and data are provided or not)?

Answer: [Yes]

Justification: We include within reasonable effort all details that one might require to reproduce our experiments, as well as linking the dataset used.

Guidelines:

- The answer [N/A] means that the paper does not include experiments.
- If the paper includes experiments, a [No] answer to this question will not be perceived well by the reviewers: Making the paper reproducible is important, regardless of whether the code and data are provided or not.
- If the contribution is a dataset and/or model, the authors should describe the steps taken to make their results reproducible or verifiable.
- Depending on the contribution, reproducibility can be accomplished in various ways. For example, if the contribution is a novel architecture, describing the architecture fully might suffice, or if the contribution is a specific model and empirical evaluation, it may be necessary to either make it possible for others to replicate the model with the same

dataset, or provide access to the model. In general, releasing code and data is often one good way to accomplish this, but reproducibility can also be provided via detailed instructions for how to replicate the results, access to a hosted model (e.g., in the case of a large language model), releasing of a model checkpoint, or other means that are appropriate to the research performed.

- While NeurIPS does not require releasing code, the conference does require all submissions to provide some reasonable avenue for reproducibility, which may depend on the nature of the contribution. For example
  - (a) If the contribution is primarily a new algorithm, the paper should make it clear how to reproduce that algorithm.
  - (b) If the contribution is primarily a new model architecture, the paper should describe the architecture clearly and fully.
  - (c) If the contribution is a new model (e.g., a large language model), then there should either be a way to access this model for reproducing the results or a way to reproduce the model (e.g., with an open-source dataset or instructions for how to construct the dataset).
  - (d) We recognize that reproducibility may be tricky in some cases, in which case authors are welcome to describe the particular way they provide for reproducibility. In the case of closed-source models, it may be that access to the model is limited in some way (e.g., to registered users), but it should be possible for other researchers to have some path to reproducing or verifying the results.

## 5. Open access to data and code

Question: Does the paper provide open access to the data and code, with sufficient instructions to faithfully reproduce the main experimental results, as described in supplemental material?

Answer: [Yes]

Justification: We provide the code used for our experiments as reference in our supplementary material. In addition to this, we intend to make our code openly available on github for the research community to reproduce our experiments on acceptance of our paper.

Guidelines:

- The answer [N/A] means that paper does not include experiments requiring code.
- Please see the NeurIPS code and data submission guidelines (<https://neurips.cc/public/guides/CodeSubmissionPolicy>) for more details.
- While we encourage the release of code and data, we understand that this might not be possible, so [No] is an acceptable answer. Papers cannot be rejected simply for not including code, unless this is central to the contribution (e.g., for a new open-source benchmark).
- The instructions should contain the exact command and environment needed to run to reproduce the results. See the NeurIPS code and data submission guidelines (<https://neurips.cc/public/guides/CodeSubmissionPolicy>) for more details.
- The authors should provide instructions on data access and preparation, including how to access the raw data, preprocessed data, intermediate data, and generated data, etc.
- The authors should provide scripts to reproduce all experimental results for the new proposed method and baselines. If only a subset of experiments are reproducible, they should state which ones are omitted from the script and why.
- At submission time, to preserve anonymity, the authors should release anonymized versions (if applicable).
- Providing as much information as possible in supplemental material (appended to the paper) is recommended, but including URLs to data and code is permitted.

## 6. Experimental setting/details

Question: Does the paper specify all the training and test details (e.g., data splits, hyperparameters, how they were chosen, type of optimizer) necessary to understand the results?

Answer: [Yes]

Justification: We provide within all reasonable effort all experimental settings and details need to reproduce our results.

Guidelines:

- The answer [N/A] means that the paper does not include experiments.
- The experimental setting should be presented in the core of the paper to a level of detail that is necessary to appreciate the results and make sense of them.
- The full details can be provided either with the code, in appendix, or as supplemental material.

## 7. Experiment statistical significance

Question: Does the paper report error bars suitably and correctly defined or other appropriate information about the statistical significance of the experiments?

Answer: [No]

Justification: Some of our experiments don't necessarily suit using error bars or statistical significance as a way of representing information.

Guidelines:

- The answer [N/A] means that the paper does not include experiments.
- The authors should answer [Yes] if the results are accompanied by error bars, confidence intervals, or statistical significance tests, at least for the experiments that support the main claims of the paper.
- The factors of variability that the error bars are capturing should be clearly stated (for example, train/test split, initialization, random drawing of some parameter, or overall run with given experimental conditions).
- The method for calculating the error bars should be explained (closed form formula, call to a library function, bootstrap, etc.)
- The assumptions made should be given (e.g., Normally distributed errors).
- It should be clear whether the error bar is the standard deviation or the standard error of the mean.
- It is OK to report 1-sigma error bars, but one should state it. The authors should preferably report a 2-sigma error bar than state that they have a 96% CI, if the hypothesis of Normality of errors is not verified.
- For asymmetric distributions, the authors should be careful not to show in tables or figures symmetric error bars that would yield results that are out of range (e.g., negative error rates).
- If error bars are reported in tables or plots, the authors should explain in the text how they were calculated and reference the corresponding figures or tables in the text.

## 8. Experiments compute resources

Question: For each experiment, does the paper provide sufficient information on the computer resources (type of compute workers, memory, time of execution) needed to reproduce the experiments?

Answer: [Yes]

Justification: We provide details about the computer resources used to run our experiments.

Guidelines:

- The answer [N/A] means that the paper does not include experiments.
- The paper should indicate the type of compute workers CPU or GPU, internal cluster, or cloud provider, including relevant memory and storage.
- The paper should provide the amount of compute required for each of the individual experimental runs as well as estimate the total compute.
- The paper should disclose whether the full research project required more compute than the experiments reported in the paper (e.g., preliminary or failed experiments that didn't make it into the paper).

## 9. Code of ethics

Question: Does the research conducted in the paper conform, in every respect, with the NeurIPS Code of Ethics <https://neurips.cc/public/EthicsGuidelines>?

Answer: [Yes]

Justification: We conform to the NeurIPS code of Ethics.

Guidelines:

- The answer [N/A] means that the authors have not reviewed the NeurIPS Code of Ethics.
- If the authors answer [No], they should explain the special circumstances that require a deviation from the Code of Ethics.
- The authors should make sure to preserve anonymity (e.g., if there is a special consideration due to laws or regulations in their jurisdiction).

#### 10. Broader impacts

Question: Does the paper discuss both potential positive societal impacts and negative societal impacts of the work performed?

Answer: [Yes]

Justification: We to some degree discuss potential positive societal impacts of the work performed, especially with regard to the downstream applications of our OSP, for example flood detection and marine area protection. However, we are limited from having a very in depth discussion on societal impacts by the 9-page page limit, considering we also have to show many experiments to prove our claims. We are not aware of any specific potential negative societal impacts of our work.

Guidelines:

- The answer [N/A] means that there is no societal impact of the work performed.
- If the authors answer [N/A] or [No], they should explain why their work has no societal impact or why the paper does not address societal impact.
- Examples of negative societal impacts include potential malicious or unintended uses (e.g., disinformation, generating fake profiles, surveillance), fairness considerations (e.g., deployment of technologies that could make decisions that unfairly impact specific groups), privacy considerations, and security considerations.
- The conference expects that many papers will be foundational research and not tied to particular applications, let alone deployments. However, if there is a direct path to any negative applications, the authors should point it out. For example, it is legitimate to point out that an improvement in the quality of generative models could be used to generate Deepfakes for disinformation. On the other hand, it is not needed to point out that a generic algorithm for optimizing neural networks could enable people to train models that generate Deepfakes faster.
- The authors should consider possible harms that could arise when the technology is being used as intended and functioning correctly, harms that could arise when the technology is being used as intended but gives incorrect results, and harms following from (intentional or unintentional) misuse of the technology.
- If there are negative societal impacts, the authors could also discuss possible mitigation strategies (e.g., gated release of models, providing defenses in addition to attacks, mechanisms for monitoring misuse, mechanisms to monitor how a system learns from feedback over time, improving the efficiency and accessibility of ML).

#### 11. Safeguards

Question: Does the paper describe safeguards that have been put in place for responsible release of data or models that have a high risk for misuse (e.g., pre-trained language models, image generators, or scraped datasets)?

Answer: [N/A]

Justification: We are not aware of any risk of misuse of our work.

Guidelines:

- The answer [N/A] means that the paper poses no such risks.

- Released models that have a high risk for misuse or dual-use should be released with necessary safeguards to allow for controlled use of the model, for example by requiring that users adhere to usage guidelines or restrictions to access the model or implementing safety filters.
- Datasets that have been scraped from the Internet could pose safety risks. The authors should describe how they avoided releasing unsafe images.
- We recognize that providing effective safeguards is challenging, and many papers do not require this, but we encourage authors to take this into account and make a best faith effort.

## 12. Licenses for existing assets

Question: Are the creators or original owners of assets (e.g., code, data, models), used in the paper, properly credited and are the license and terms of use explicitly mentioned and properly respected?

Answer: [Yes]

Justification: We use open source data from ESA's Sentinel-1 satellites for our model training and experiments. Other than this we don't use any other assets. Any theoretical concepts that we use are mentioned and referenced in our paper.

Guidelines:

- The answer [N/A] means that the paper does not use existing assets.
- The authors should cite the original paper that produced the code package or dataset.
- The authors should state which version of the asset is used and, if possible, include a URL.
- The name of the license (e.g., CC-BY 4.0) should be included for each asset.
- For scraped data from a particular source (e.g., website), the copyright and terms of service of that source should be provided.
- If assets are released, the license, copyright information, and terms of use in the package should be provided. For popular datasets, [paperswithcode.com/datasets](https://paperswithcode.com/datasets) has curated licenses for some datasets. Their licensing guide can help determine the license of a dataset.
- For existing datasets that are re-packaged, both the original license and the license of the derived asset (if it has changed) should be provided.
- If this information is not available online, the authors are encouraged to reach out to the asset's creators.

## 13. New assets

Question: Are new assets introduced in the paper well documented and is the documentation provided alongside the assets?

Answer: [N/A]

Justification: We don't release any new assets, accept for the code itself, which we will release on github upon acceptance.

Guidelines:

- The answer [N/A] means that the paper does not release new assets.
- Researchers should communicate the details of the dataset/code/model as part of their submissions via structured templates. This includes details about training, license, limitations, etc.
- The paper should discuss whether and how consent was obtained from people whose asset is used.
- At submission time, remember to anonymize your assets (if applicable). You can either create an anonymized URL or include an anonymized zip file.

## 14. Crowdsourcing and research with human subjects

Question: For crowdsourcing experiments and research with human subjects, does the paper include the full text of instructions given to participants and screenshots, if applicable, as well as details about compensation (if any)?

Answer: [N/A]

Justification: We do not perform any research with human subjects.

Guidelines:

- The answer [N/A] means that the paper does not involve crowdsourcing nor research with human subjects.
- Including this information in the supplemental material is fine, but if the main contribution of the paper involves human subjects, then as much detail as possible should be included in the main paper.
- According to the NeurIPS Code of Ethics, workers involved in data collection, curation, or other labor should be paid at least the minimum wage in the country of the data collector.

**15. Institutional review board (IRB) approvals or equivalent for research with human subjects**

Question: Does the paper describe potential risks incurred by study participants, whether such risks were disclosed to the subjects, and whether Institutional Review Board (IRB) approvals (or an equivalent approval/review based on the requirements of your country or institution) were obtained?

Answer: [N/A]

Justification: We do not perform any research that would require IRB approval. We do not do any research on human subjects.

Guidelines:

- The answer [N/A] means that the paper does not involve crowdsourcing nor research with human subjects.
- Depending on the country in which research is conducted, IRB approval (or equivalent) may be required for any human subjects research. If you obtained IRB approval, you should clearly state this in the paper.
- We recognize that the procedures for this may vary significantly between institutions and locations, and we expect authors to adhere to the NeurIPS Code of Ethics and the guidelines for their institution.
- For initial submissions, do not include any information that would break anonymity (if applicable), such as the institution conducting the review.

**16. Declaration of LLM usage**

Question: Does the paper describe the usage of LLMs if it is an important, original, or non-standard component of the core methods in this research? Note that if the LLM is used only for writing, editing, or formatting purposes and does *not* impact the core methodology, scientific rigor, or originality of the research, declaration is not required.

Answer: [N/A]

Justification: The core method development in this research does not involve LLMs as any important, original or non-standard components.

Guidelines:

- The answer [N/A] means that the core method development in this research does not involve LLMs as any important, original, or non-standard components.
- Please refer to our LLM policy in the NeurIPS handbook for what should or should not be described.